

Resolvent-based estimation and control of a laminar airfoil wake

Junoh Jung^{*1}, Rutvij Bhagwat^{1, 2}, Aaron Towne¹

¹Department of Mechanical Engineering, University of Michigan, Ann Arbor, MI, USA

²Department of Mechanical Engineering, Florida State University, Tallahassee, FL 32310, USA

Abstract. We develop an optimal resolvent-based estimator and controller to predict and attenuate unsteady vortex shedding fluctuations in the laminar wake of a NACA 0012 airfoil at an angle of attack of 6.5 degrees, chord-based Reynolds number of 5000, and Mach number of 0.3. The resolvent-based estimation and control framework offers several advantages over standard methods. Under equivalent assumptions, the resolvent-based estimator and controller reproduce the Kalman filter and LQG controller, respectively, but at substantially lower computational cost using either an operator-based or data-driven implementation. Unlike these methods, the resolvent-based approach can naturally accommodate forcing terms (nonlinear terms from Navier-Stokes) with colored-in-time statistics, significantly improving estimation accuracy and control efficacy. Causality is optimally enforced using a Wiener-Hopf formalism. We integrate these tools into a high-performance-computing-ready compressible flow solver and demonstrate their effectiveness for estimating and controlling velocity fluctuations in the wake of the airfoil immersed in clean and noisy freestreams, the latter of which prevents the flow from falling into a periodic limit cycle. Using four shear-stress sensors on the surface of the airfoil, the resolvent-based estimator predicts a series of downstream targets with approximately 3% and 30% error for the clean and noisy freestream conditions, respectively. For the latter case, using four actuators on the airfoil surface, the resolvent-based controller reduces the turbulent kinetic energy in the wake by 98%.

1 Introduction

The laminar flow over an airfoil is a canonical problem in fluid mechanics due to its role in aerodynamics and status as a prototypical problem for studying wakes. Unsteady perturbations in the wake are of particular interest for several reasons. First, these perturbations are intimately tied to the separation bubble that forms over the suction side of the airfoil, which in turn increases drag [Alam et al., 2010, Chang et al., 2022]. Second, unsteady fluctuations can degrade aerodynamic performance in many aircraft flight control scenarios, such as maneuvers at high angles of attack, landing, takeoff, or encountering atmospheric turbulence. Third, wake perturbations significantly contribute to aerodynamic noise, which is a concern for wind turbines [Wagner et al., 1996, Agrawal et al., 2015] and rotorcrafts, including drones. In all these scenarios, accurate estimation and effective closed-loop control of wake perturbations are critical to improve engineering performance, i.e., to reduce drag, enhance flight control, and mitigate aerodynamic noise.

A dominant feature of the laminar flow over an airfoil is vortex shedding in the wake. Vortices form on

*Email address for correspondence: junohj@umich.edu

each side of the airfoil and shed periodically, creating downstream flow patterns such as the Karman vortex street. Factors including the shape of the object, the angle of attack, and the Reynolds number influence this vortex shedding. In NACA0012 airfoils at moderate angles of attack (6-10 degrees), an anticlockwise vortex is generated at the trailing edge, and a clockwise vortex at the front suction side separates and is entrained downstream [Chang et al., 2022] – accordingly, both the front section of the suction side and the trailing edge impact vortex-shedding. Many studies have been conducted to suppress vortex shedding in the wakes behind cylinders [Jin et al., 2020, Déda et al., 2023, Lin and Tsai, 2024] and airfoils [Colonius and Williams, 2011, Broglia et al., 2018].

An accurate estimator is essential for successful closed-loop control [Stengel, 1994, Brunton and Noack, 2015]. Standard estimation and control methods such as the Kalman filter [Kalman, 1960] and the linear-quadratic-Gaussian (LQG) controller have been applied to fluid mechanics problems over the past two decades, e.g., Kalman filter [Rafiee et al., 2009, Colburn et al., 2011, An et al., 2021] and LQG control [Bagheri et al., 2009, Fabbiane et al., 2014, 2015, 2017, Sasaki et al., 2018a]. However, these standard methods have two significant limitations when applied to flow-control problems. First, solving the Riccati equations required to obtain the Kalman and LQG gains scales poorly with problem size and becomes computationally expensive, or in some cases prohibitive, for the large systems typically obtained when discretizing the Navier-Stokes equations. This issue can be partially mitigated by reducing the size of the system a priori via some model-reduction method [Pasquale et al., 2017, Gomez et al., 2019], but this potentially degrades the performance of the controller. Second, standard methods model the nonlinear terms of the Navier-Stokes equations as a white noise forcing on the linear dynamics. These terms are not white [Zare et al., 2017, Towne et al., 2017, Morra et al., 2021], and treating them as such deteriorates estimation and control performance [Martini et al., 2020, Amaral et al., 2021].

In this paper, we utilize a recently developed class of estimation and control methods based on resolvent analysis [Towne et al., 2020, Martini et al., 2020, 2022]. Resolvent analysis, or input-output analysis, is a powerful methodology based on a linear mapping between forcing (input) and response (output) modes and the gain between them. These modes and gains are obtained from a singular value decomposition of the resolvent operator obtained from the linearized Navier-Stokes equations. Early studies viewed the input as an external forcing on the Navier-Stokes equations linearized about some laminar fixed point [Jovanović and Bamieh, 2005, Sharma et al., 2006, Sipp et al., 2010]. McKeon and Sharma [2010] extended resolvent analysis to turbulent flows by interpreting the nonlinear terms from the Navier-Stokes equations as a forcing on the linear dynamics. Towne et al. [2018] showed that resolvent modes and spectral proper orthogonal decomposition (SPOD) modes are identical when the forcing is white noise, directly linking resolvent modes to coherent structures observed in flow data. However, resolvent analysis poses computational challenges for high-dimensional problems. To address these difficulties, Ribeiro et al. [2020] applied randomized SVD. Martini et al. [2020] used a time-stepping approach to obtain the action of the resolvent operator on a specified forcing, eliminating the need to compute the inverse of large matrices. Farghadan et al. [2023, 2024] further extended the range of problems amenable to resolvent analysis by combining randomized SVD with an approach to minimize the cost of the time-stepping method and successfully applied the method to several three-dimensional problems.

Resolvent analysis has been extensively used to study the flow over airfoils at different Reynolds numbers and angles of attack. Thomareis and Papadakis [2018] investigated the physics of separated and attached flows around a NACA 0012 airfoil at $Re_{L_c} = 50,000$ and angle of attack 5° . Symon et al. [2019] investigated two angles of attack, 0° and 10° , for a NACA 0018 airfoil and showed that these two cases behave as an oscillator and amplifier [Huerre and Monkewitz, 1990], respectively. Kojima et al. [2020] identified the origin of the two-dimensional transonic buffet over a NACA 0012 airfoil at $Re_{L_c} = 2,000$, $Ma_\infty = 0.85$ and $\alpha = 3^\circ$. Marquet et al. [2022] studied the flow over a NACA 0012 at $Re_{L_c} = 5,000$ for angles of attack between $\alpha = 6.5^\circ$ and 9° using an incompressible Navier-Stokes linear operator with the mean flow obtained from a numerical simulation, which was validated against experimental data.

Motivated by the ability of resolvent modes to efficiently represent coherent structures, [Towne et al. \[2020\]](#) introduced a resolvent-based method to estimate space-time flow statistics from limited sensor measurements. [Martini et al. \[2020\]](#) extended this method to reconstruct the time series of the flow state using limited measurements. [Amaral et al. \[2021\]](#) used this method to estimate the velocity field in a channel flow using pressure and shear-stress measurements at the channel wall. The aforementioned resolvent-based estimators are non-causal, i.e., they use both past and future measurements to determine the current flow state. [Martini et al. \[2022\]](#) derived a causal resolvent-based estimator and controller by enforcing causality using a Wiener-Hopf formalism [[Martinelli, 2009](#)], making them applicable for closed-loop flow control.

The causal resolvent-based estimator and controller reproduce the Kalman filter and LQG controller, respectively, under equivalent assumptions, namely white-noise forcing. However, the resolvent-based estimator and controller have two crucial advantages over these standard methods. First, they can be efficiently computed even for large systems using a time-stepping method similar to that described earlier for computing resolvent modes or via a data-driven approach. This makes the method applicable to the large problems typical of fluid mechanics without the need for detrimental a priori model reduction. Second, the resolvent-based methods can accommodate colored-in-time forcing to statistically account for the nonlinear terms from the Navier-Stokes equations, improving estimation accuracy and control efficacy.

In this paper, we aim to estimate and control unsteady fluctuations in the wake of a two-dimensional NACA 0012 airfoil at $Ma_\infty = 0.3$, $Re_{L_c} = 5000$, and $\alpha = 6.5^\circ$ using the resolvent-based methods. The overall roadmap of the paper is depicted schematically in figure 1. We begin in § 2 by computing the flow using direct numerical simulation (DNS) and validate the simulation against results in the literature. In § 3, we analyze the global eigenmodes and resolvent modes of the flow to validate the linearized compressible Navier-Stokes operator and highlight the key flow physics. We then introduce the resolvent-based estimation and control methods in § 4, discuss how the kernels are computed in § 5, and detail our implementation of these tools into a computational fluids dynamics (CFD) code in § 6. The resolvent-based estimator is applied to both the linearized and nonlinear problems for clean and noisy freestream conditions, the latter of which is designed to disrupt the periodic vortex-shedding and induce chaotic fluctuations in the wake, in § 7. Following this, we demonstrate the effectiveness of resolvent-based control for the same systems and flow conditions in § 8. Finally, § 9 summarizes the paper and discusses future research directions.

2 Problem setup and simulation

We aim to use a resolvent-based approach to estimate and mitigate chaotic velocity fluctuations in a laminar airfoil wake. Following [Marquet et al. \[2022\]](#), we consider the flow around a NACA0012 airfoil at a low chord-based Reynolds number of $Re_{L_c} = 5000$, Mach number of $Ma_\infty = 0.3$, and an angle of attack of $\alpha = 6.5^\circ$. We consider two different freestream conditions: (i) a clean freestream with no ambient fluctuations and (ii) a noisy freestream with substantial ambient fluctuations generated by random forcing upstream of the airfoil. The flow falls into a periodic limit cycle due to vortex shedding for the clean freestream; the noisy freestream kicks the flow out of this limit cycle, leading to chaotic fluctuations in the wake – a far more challenging problem for estimation and control.

We simulate the flow via a direct numerical simulation (DNS) using the compressible flow solver CharLES [[Brès et al., 2017](#)]. A C-shape mesh is created using Pointwise, as shown in figure 2(a), where the computational grid near the airfoil is also shown in the red box. The leading edge of the airfoil is located at the origin, $x/L_c = y/L_c = 0$. The size of the domain in the streamwise and normal direction is $x/L_c \in [-49, 50]$ and $y/L_c \in [-50, 50]$, respectively. To create a two-dimensional simulation, the spanwise direction is one cell thick ($z/L_c \in [0, 0.1]$) with symmetry boundary conditions. The grid consists of approximately 148,000 cells, with a finer grid resolution applied in the wake region, as studied in appendix B. Characteristic far-field boundary conditions are applied along the outer boundary of the domain, and a

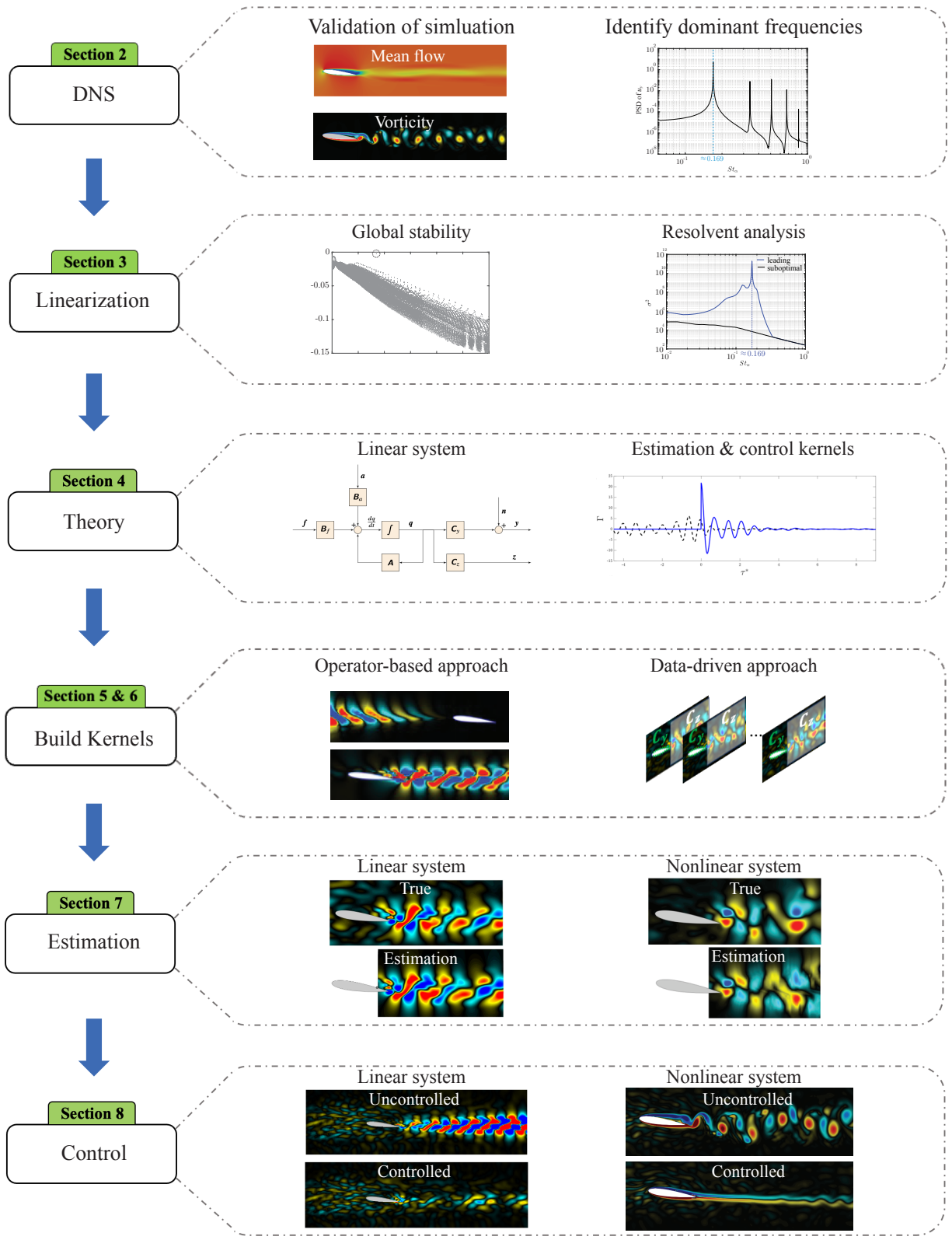


FIGURE 1: Roadmap for resolvent-based estimation and control of the laminar flow over an airfoil.

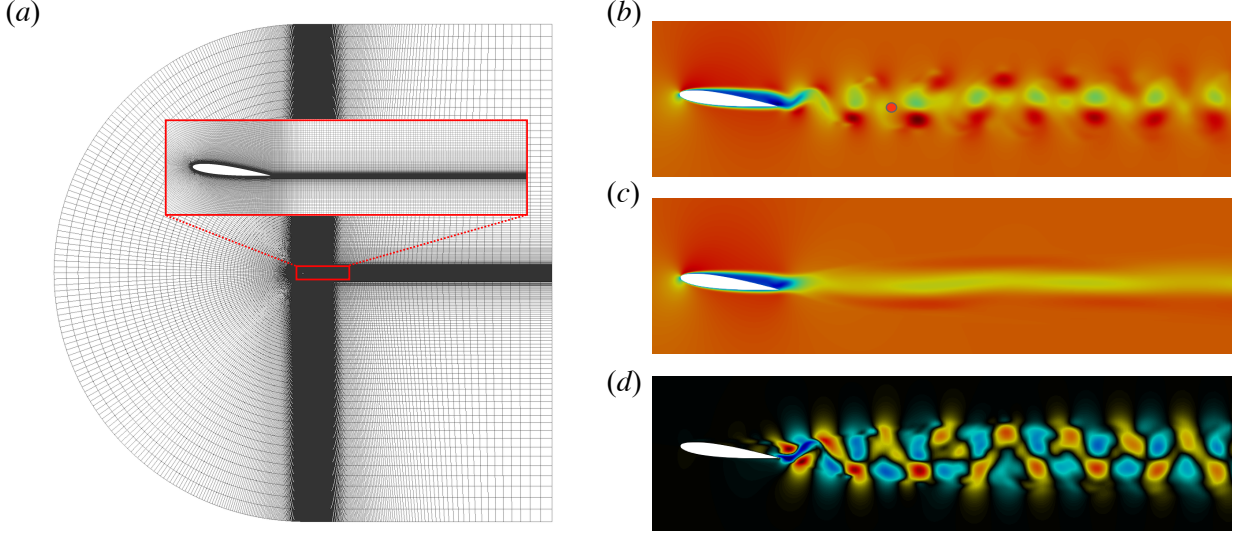


FIGURE 2: Direct numerical simulation: (a) the full computational C-shaped grid with a close-up view for the wall and wake regions, (b) a snapshot of the instantaneous streamwise velocity u_x with the red dot indicating the probe location at $(x, y)/L_c = (2.1, -0.11)$ for the power spectral density in figure 3, (c) the mean streamwise velocity \bar{u}_x , and (d) a snapshot of the instantaneous streamwise velocity fluctuation u'_x .

sponge layer is used in the region $x/L_c \in [30, 50]$ to prevent reflections and ensure an effective outflow boundary condition as the wake exits the domain. Time integration is performed using a third-order total-variation-diminishing Runge-Kutta scheme [Gottlieb and Shu, 1998]. A constant timestep is maintained by setting the Courant–Friedrichs–Lewy (CFL) number to approximately 1. After passing initial transients, data are collected for the duration $tU_\infty/L_c \in [0, 350]$. This extended time window ensures convergence of the mean and the second-order space-time statistics of vortex shedding in the wake.

Figure 2(b) shows an instantaneous snapshot of the streamwise velocity field around the airfoil. A separation bubble on the suction side of the airfoil and vortex shedding in the wake are clearly observed. The mean streamwise velocity is shown in Figure 2(c). This mean flow (along with the mean of the other state variables) is used to define the linearization used to construct the estimation and control kernels. Figure 2(d) shows an instantaneous snapshot of the streamwise velocity fluctuation, i.e., the mean-subtracted velocity. We aim to estimate and control (suppress) such fluctuations.

We validate the DNS via comparisons of the aerodynamic forces and vortex-shedding frequency against the results of Marquet et al. [2022], who considered incompressible flow over the same airfoil at the same Reynolds number and angle of attack. The time-averaged drag and lift coefficients,

$$C_D = \frac{F_D}{\frac{1}{2}\rho_\infty U_\infty^2 A}, C_L = \frac{F_L}{\frac{1}{2}\rho_\infty U_\infty^2 A}, \quad (2.1)$$

are reported in Table 1. Our results match those of Marquet et al. [2022] within a 2% error. The power spectral density (PSD) of the transverse velocity at $x/L_c = 2.1, y/L_c = -0.11$ is shown in figure 3. The vortex-shedding frequency $St_\alpha \equiv \omega_r(L_c \sin\alpha)/(2\pi Ma_\infty)$ is approximately 0.169 in the present study, close to the value of 0.18 found by Marquet et al. [2022]. This slight difference in the aerodynamic forces and vortex-shedding frequency could result from minor differences between the incompressible and compressible flows or differences in the grid refinement (the present grid is more finely resolved).

	Present study	Marquet et al. [2022]	Error
\bar{C}_D	0.0862	0.088	2.05%
\bar{C}_L	0.2941	0.289	1.76%

TABLE 1: The comparison of the time-averaged drag and lift coefficients at $\alpha = 6.5^\circ$ with the results from incompressible periodic solution for a NACA 0012 airfoil at $Re_{L_c} = 5,000$ and $Ma_\infty = 0.3$.

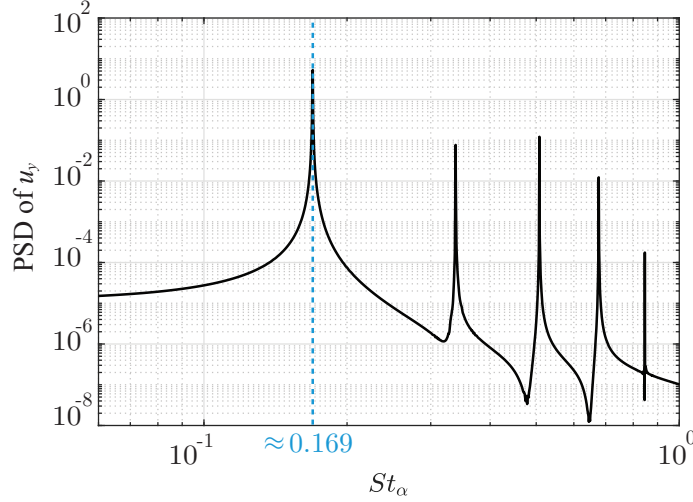


FIGURE 3: Power spectral density (PSD) of the wall-normal velocity at $(x, y)/L_c = (2.1, -0.11)$.

3 Global stability and resolvent analyses

3.1 Linearization and global stability analysis

We start with the compressible Navier-Stokes equations written as

$$\frac{\partial \mathbf{q}}{\partial t} = \mathcal{F}(\mathbf{q}), \quad (3.1)$$

where \mathbf{q} is a state vector of flow variables $[\rho, \rho u_x, \rho u_y, \rho u_z, \rho E]^T$ and \mathcal{F} is the nonlinear Navier-Stokes operator. The equations are linearized using a Reynolds decomposition, giving

$$\frac{\partial \mathbf{q}'}{\partial t} - \mathbf{A} \mathbf{q}' = \mathbf{B} \mathbf{f}(\bar{\mathbf{q}}, \mathbf{q}'), \quad (3.2)$$

where $\bar{\mathbf{q}}$ and \mathbf{q}' represent the mean and perturbation state vectors, respectively, $\mathbf{A} = \frac{\partial \mathcal{F}(\bar{\mathbf{q}})}{\partial \mathbf{q}}$ is the linearized Navier-Stokes operator, \mathbf{f} comprises the remaining nonlinear terms and any exogenous forcing, and \mathbf{B} is an input matrix that can be used to restrict the form of \mathbf{f} . For convenience, we omit $(\cdot)'$ for perturbation from this point on. Our approach for constructing \mathbf{A} is detailed in §6.

Resolvent-based estimation and control are nominally applicable and robust only for globally stable systems [Schmid and Sipp, 2016, Martini et al., 2020, 2022]. Thus, we first conduct a global stability analysis to ensure that our linear operator is stable. Figure 4(a) shows the spectrum of the linearized Navier-Stokes operator \mathbf{A} , represented in terms of the complex frequency $\omega = i\lambda$, where λ is the eigenvalue of \mathbf{A} . The imaginary part ω_i is negative for all eigenvalues, indicating that the flow around the airfoil is globally stable. The least-damped eigenvalue appears at the frequency $St_\alpha \approx 0.169$, which matches the

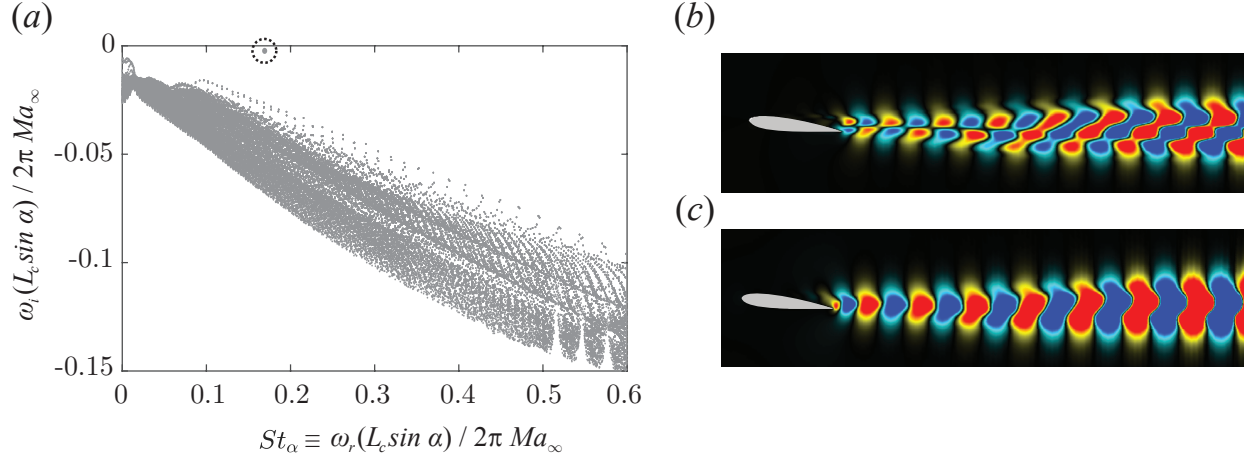


FIGURE 4: Eigenspectrum: (a) Eigenspectrum. The dotted circle shows the dominant wake eigenmode at the vortex-shedding frequency $St_\alpha \approx 0.17$, (b) the corresponding streamwise velocity eigenmode, and (c) cross-streamwise velocity eigenmode.

vortex-shedding frequency observed in the PSD in figure 3. The corresponding eigenmode, shown in 4(b) and (c), exhibits the expected characteristics of vortex shedding [Noack et al., 2003].

3.2 Resolvent analysis

Resolvent analysis is central to our estimation and control methods. Therefore, we compute the leading resolvent modes for the airfoil flow as a preliminary step to validate our implementation and to gain insights into the flow physics and the appropriate sensor and actuator placements. After transforming the linear system (3.2) into the frequency domain and solving for the state, we obtain

$$\hat{q} = \mathbf{R}\mathbf{B}\hat{f}, \quad (3.3)$$

where the resolvent operator is defined as $\mathbf{R} = (-i\omega\mathbf{I} - \mathbf{A})^{-1}$. The notation $(\hat{\cdot})$ indicates a quantity in the frequency domain throughout this paper.

Resolvent analysis seeks input and output modes that maximize the resolvent gain

$$\sigma^2 = \frac{\|\hat{y}\|^2}{\|\hat{f}\|^2}, \quad (3.4)$$

where $\hat{y} = \mathbf{C}\hat{q}$ is an output of interest extracted from the state by the output matrix \mathbf{C} . The norm is induced by the inner product $\langle q_1, q_2 \rangle = q_1^* \mathbf{W} q_2$, where \mathbf{W} is a weight matrix used to set a desired norm and $(\cdot)^*$ indicates the conjugate transpose. We use the Chu compressible energy norm [Chu, 1965] and set \mathbf{B} and \mathbf{C} to the identity matrix for the preliminary resolvent analysis in this section (non-identity values will be used later for estimation and control).

After defining the weighted resolvent operator

$$\tilde{\mathbf{R}} = \mathbf{W}^{\frac{1}{2}} \mathbf{C} \mathbf{R} \mathbf{B} \mathbf{W}^{-\frac{1}{2}}, \quad (3.5)$$

the resolvent gains and modes are obtained from the SVD

$$\tilde{\mathbf{R}} = \tilde{\mathbf{U}} \tilde{\Sigma} \tilde{\mathbf{V}}^*. \quad (3.6)$$

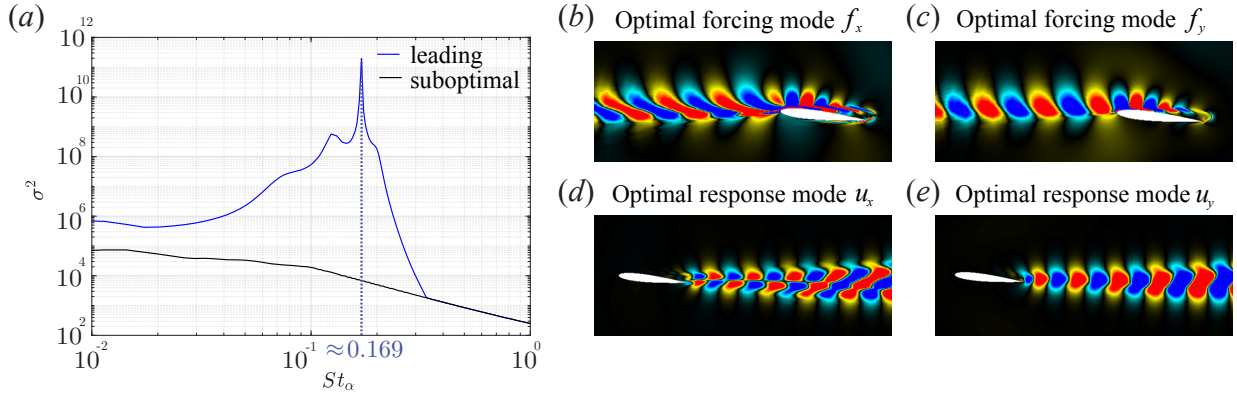


FIGURE 5: Resolvent gains, optimal forcing and response modes: (a) leading and second optimal gains, (b) optimal forcing mode of u_x , (c) optimal forcing mode of u_y , (d) optimal response mode of u_x , and (e) optimal response mode of u_y .

The resolvent gains are contained within the diagonal matrix $\Sigma = \text{diag}[\sigma_1, \sigma_2, \dots, \sigma_n]$. The forcing and response modes that maximize (3.4) are recovered as $\mathbf{V} = \mathbf{W}^{-\frac{1}{2}}\tilde{\mathbf{V}}$ and $\mathbf{U} = \mathbf{W}^{-\frac{1}{2}}\tilde{\mathbf{U}}$, respectively Towne et al. [2018]. We compute the resolvent modes by transforming the SVD into an equivalent eigenvalue problem, which is solved using an Arnoldi iteration in which The action of $\tilde{\mathbf{R}}$ is obtained by computing its LU decomposition [Jeun et al., 2016, Schmidt et al., 2018].

In figure 5, the peak of the leading resolvent gain is observed at the vortex shedding frequency $St_\alpha \approx 0.169$. The streamwise and transverse velocity components of the optimal forcing and response modes are shown in figure 5(b)-(e). The optimal forcing mode is primarily located upstream and above the airfoil, while the optimal response mode is clearly observed downstream in the wake, as expected for a convective flow. The optimal response mode is similar to the dominant eigenmode.

4 Resolvent-based estimation and control framework

In this section, we provide a brief overview of the resolvent-based estimation and control framework developed by Towne et al. [2020] and Martini et al. [2020, 2022].

4.1 System set-up

As a generalization of (3.2), we consider the linear time-invariant system

$$\frac{d\mathbf{q}}{dt}(t) = \mathbf{A}\mathbf{q}(t) + \mathbf{B}_f\mathbf{f}(t) + \mathbf{B}_a\mathbf{a}(t), \quad (4.1a)$$

$$\mathbf{y}(t) = \mathbf{C}_y\mathbf{q}(t) + \mathbf{n}(t), \quad (4.1b)$$

$$\mathbf{z}(t) = \mathbf{C}_z\mathbf{q}(t). \quad (4.1c)$$

The system matrix $\mathbf{A} \in \mathbb{C}^{n \times n}$ is the linearized compressible Navier-Stokes operator, $\mathbf{q} \in \mathbb{C}^n$ is the full state of flow, and n is the total size of the state. The forcing $\mathbf{f} \in \mathbb{C}^{n_f}$ represents the nonlinear terms from the Navier-Stokes equations and any exogenous forcing. The forcing matrix $\mathbf{B}_f \in \mathbb{C}^{n \times n_f}$ restricts the form of the forcing \mathbf{f} , e.g., localizes it to a certain spatial region. The actuation signal $\mathbf{a} \in \mathbb{C}^{n_a}$, which will be the output of the controller, is mapped onto the system by the actuation matrix $\mathbf{B}_a \in \mathbb{C}^{n \times n_a}$, and n_a is the total number of actuators. The sensor measurement $\mathbf{y} \in \mathbb{C}^{n_y}$ is extracted from the state by the measurement

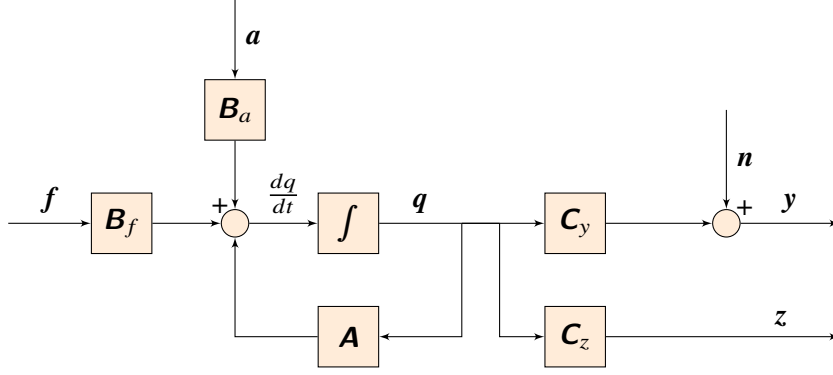


FIGURE 6: Block-diagram representation of the linear system.

matrix $\mathbf{C}_y \in \mathbb{C}^{n_y \times n_y}$, which defines the sensor locations and types, and n_y is the total number of sensors. The sensor measurements are corrupted by the sensor noise $\mathbf{n} \in \mathbb{C}^{n_y}$. The target $\mathbf{z} \in \mathbb{C}^{n_z}$, i.e., the quantity that we wish to estimate and control, is extracted from the state by the target matrix $\mathbf{C}_z \in \mathbb{C}^{n_z \times n_z}$, and n_z is the total number of targets.

Following [Martini et al. \[2022\]](#), we split the system (4.1) into two parts: the so-called forcing system that is driven by the forcing $\mathbf{f}(t)$ and corrupted by the sensor noise $\mathbf{n}(t)$,

$$\frac{d\mathbf{q}_f}{dt}(t) = \mathbf{A}\mathbf{q}_f(t) + \mathbf{B}_f\mathbf{f}(t), \quad (4.2a)$$

$$\mathbf{y}_f(t) = \mathbf{C}_y\mathbf{q}_f(t) + \mathbf{n}(t), \quad (4.2b)$$

$$\mathbf{z}_f(t) = \mathbf{C}_z\mathbf{q}_f(t), \quad (4.2c)$$

and the actuation system that is driven only by the actuation signal $\mathbf{a}(t)$,

$$\frac{d\mathbf{q}_a}{dt}(t) = \mathbf{A}\mathbf{q}_a(t) + \mathbf{B}_a\mathbf{a}(t), \quad (4.3a)$$

$$\mathbf{y}_a(t) = \mathbf{C}_y\mathbf{q}_a(t), \quad (4.3b)$$

$$\mathbf{z}_a(t) = \mathbf{C}_z\mathbf{q}_a(t). \quad (4.3c)$$

The state, sensor measurements, and targets for the full system are recovered as

$$\mathbf{q} = \mathbf{q}_f + \mathbf{q}_a, \quad \mathbf{y} = \mathbf{y}_f + \mathbf{y}_a, \quad \text{and} \quad \mathbf{z} = \mathbf{z}_f + \mathbf{z}_a. \quad (4.4)$$

By applying the Fourier transform to (4.2) and (4.3) and using the resolvent operator defined in (3.3), we obtain the frequency-domain representations of sensor measurements and targets of the forcing and actuation systems,

$$\hat{\mathbf{y}}_f = \mathbf{R}_{y_f}\hat{\mathbf{f}} + \hat{\mathbf{n}}, \quad (4.5a)$$

$$\hat{\mathbf{z}}_f = \mathbf{R}_{z_f}\hat{\mathbf{f}}, \quad (4.5b)$$

$$\hat{\mathbf{y}}_a = \mathbf{R}_{y_a}\hat{\mathbf{a}}, \quad (4.5c)$$

$$\hat{\mathbf{z}}_a = \mathbf{R}_{z_a}\hat{\mathbf{a}}. \quad (4.5d)$$

Here, $\mathbf{R}_{y_f} = \mathbf{C}_y\mathbf{R}\mathbf{B}_f$, $\mathbf{R}_{z_f} = \mathbf{C}_z\mathbf{R}\mathbf{B}_f$, $\mathbf{R}_{y_a} = \mathbf{C}_y\mathbf{R}\mathbf{B}_a$, and $\mathbf{R}_{z_a} = \mathbf{C}_z\mathbf{R}\mathbf{B}_a$ are modified resolvent operators (sometimes called input-output operators) that will appear in the resolvent-based estimation and control kernels.

4.2 Resolvent-based estimation

The resolvent-based estimates of the target \tilde{z} are obtained via a convolution between the sensor measurements and a kernel. Here, we define three distinct resolvent-based estimation kernels: non-causal, truncated non-causal, and causal kernels.

First, we define a non-causal estimator

$$\tilde{z}_{nc}(t) = \int_{-\infty}^{\infty} \mathbf{T}_{nc}(t - \tau) \mathbf{y}(\tau) d\tau, \quad (4.6)$$

where $\mathbf{T}_{nc} \in \mathbb{C}^{n_z \times n_y}$ is a non-causal estimation kernel. The optimal estimation kernel is obtained by minimizing a cost function defined as the time-integrated expected value of the estimation error,

$$J_{nc} = \int_{-\infty}^{\infty} \mathbb{E}\{\mathbf{e}(t)^\dagger \mathbf{e}(t)\} dt, \quad (4.7)$$

where the estimation error $\mathbf{e}(t) = \tilde{z}(t) - z(t)$ is the difference between the estimated and true target, $(\cdot)^\dagger$ denotes the adjoint operator using a suitable inner product, and $\mathbb{E}\{\cdot\}$ is the expectation operator. The cost function J_{nc} is minimized by setting its derivative with respect to \mathbf{T}_{nc} to zero, yielding the optimal non-causal estimation kernel [Martini et al., 2020]

$$\hat{\mathbf{T}}_{nc}(\omega) = \mathbf{R}_{zf} \hat{\mathbf{F}} \mathbf{R}_{yf}^\dagger (\mathbf{R}_{yf} \hat{\mathbf{F}} \mathbf{R}_{yf}^\dagger + \hat{\mathbf{N}})^{-1}, \quad (4.8)$$

where $\hat{\mathbf{F}} = \mathbb{E}\{\hat{\mathbf{f}}\hat{\mathbf{f}}^\dagger\}$ and $\hat{\mathbf{N}} = \mathbb{E}\{\hat{\mathbf{n}}\hat{\mathbf{n}}^\dagger\}$ are the CSDs of the forcing and sensor noise, respectively. The time-domain estimation kernel \mathbf{T}_{nc} is obtained by inverse Fourier transforming the frequency domain kernel $\hat{\mathbf{T}}_{nc}$. In general, this kernel will be non-causal, i.e., $\mathbf{T}_{nc}(\tau)$ will not be strictly zero for $\tau < 0$, therefore requiring future sensor data, $\mathbf{y}(\tau > 0)$, which is unavailable for real-time applications, to evaluate (4.6).

Second, we define a truncated non-causal estimation kernel as a simple baseline approach to address the aforementioned lack of causality. This is done by simply truncating the integral in (4.6),

$$\tilde{z}_{tnc}(t) = \int_{-\infty}^0 \mathbf{T}_{tnc}(t - \tau) \mathbf{y}(\tau) d\tau, \quad (4.9)$$

which is equivalent to truncating the non-causal part of the kernel,

$$\mathbf{T}_{tnc}(\tau) = \begin{cases} \mathbf{T}_{nc}(\tau), & \tau \geq 0, \\ 0, & \tau < 0. \end{cases} \quad (4.10)$$

The downside of this approach is that the ex post facto truncation of the optimal non-causal kernel ruins its optimality.

Third, we define an optimal causal resolvent-based estimation kernel by enforcing causality using the Wiener-Hopf formalism [Martinelli, 2009, Martini et al., 2022]. The causal estimator

$$\tilde{z}_c(t) = \int_{-\infty}^0 \mathbf{T}_c(t - \tau) \mathbf{y}(\tau) d\tau, \quad (4.11)$$

is defined in terms of the causal estimation kernel $\mathbf{T}_c \in \mathbb{C}^{n_z \times n_y}$. To find the optimal kernel under the constraint of causality, we modify the cost function (4.7) to read

$$J_c = \int_{-\infty}^{\infty} \mathbb{E}\{\mathbf{e}(t)^\dagger \mathbf{e}(t)\} + (\mathbf{A}_-(t) \mathbf{T}_c(t) + \mathbf{A}_-^\dagger(t) \mathbf{T}_c^\dagger(t)) dt, \quad (4.12)$$

where Λ is a Lagrange multiplier that is used to force the causal kernel to be zero for the non-causal part ($\tau < 0$). The (+) and (-) subscripts indicate that the non-causal ($\tau < 0$) and causal ($\tau > 0$) parts, respectively, of a matrix or function are set to zero using a Wiener-Hopf factorization. An introduction to the Wiener-Hopf method is described in appendix B. Similar to the derivation of (4.8), we minimize the causal cost function (4.12) by setting its derivative with respect to \mathbf{T}_c to zero. In doing so, we encounter the Wiener-Hopf problem (B.4) with $\hat{\mathbf{G}} = \mathbf{R}_{zf} \hat{\mathbf{F}} \mathbf{R}_{yf}^\dagger$ and $\hat{\mathbf{H}} = \mathbf{R}_{yf} \hat{\mathbf{F}} \mathbf{R}_{yf}^\dagger + \hat{\mathbf{N}}$. Using the solution of this Wiener-Hopf problem given by (B.8), the causal estimation kernel [Martini et al., 2022] is

$$\hat{\mathbf{T}}_c(\omega) = \left(\mathbf{R}_{zf} \hat{\mathbf{F}} \mathbf{R}_{yf}^\dagger (\mathbf{R}_{yf} \hat{\mathbf{F}} \mathbf{R}_{yf}^\dagger + \hat{\mathbf{N}})^{-1} \right)_+ \left(\mathbf{R}_{yf} \hat{\mathbf{F}} \mathbf{R}_{yf}^\dagger + \hat{\mathbf{N}} \right)_+^{-1}. \quad (4.13)$$

4.3 Resolvent-based control

Analogous to the estimation problem, the actuation signal $\mathbf{a}(t)$ that will be used to control the flow is obtained via a convolution between the sensor measurements and a control kernel (also referred to as control law in some studies). Again, we consider non-causal, truncated non-causal, and causal variations of the resolvent-based control kernels [Martini et al., 2022].

The non-causal controller takes the form

$$\mathbf{a}_{nc}(t) = \int_{-\infty}^{\infty} \boldsymbol{\Gamma}_{nc}(t - \tau) \mathbf{y}_f(\tau) d\tau, \quad (4.14)$$

where $\boldsymbol{\Gamma}_{nc} \in \mathbb{C}^{n_a \times n_y}$ is the noncausal control kernel. The optimal kernel is obtained by minimizing the cost function

$$J_{nc} = \int_{-\infty}^{\infty} \mathbb{E}\{\mathbf{z}(t)^\dagger \mathbf{z}(t) + \mathbf{a}(t)^\dagger \mathbf{P} \mathbf{a}(t)\} dt, \quad (4.15)$$

where \mathbf{P} is a weight matrix that penalizes the actuation effort. Minimizing this cost function yields the optimal non-causal control kernel

$$\hat{\boldsymbol{\Gamma}}_{nc}(\omega) = (\mathbf{R}_{za}^\dagger \mathbf{R}_{za} + \hat{\mathbf{P}})^{-1} (-\mathbf{R}_{za}^\dagger) \mathbf{R}_{zf} \hat{\mathbf{F}} \mathbf{R}_{yf}^\dagger (\mathbf{R}_{yf} \hat{\mathbf{F}} \mathbf{R}_{yf}^\dagger + \hat{\mathbf{N}})^{-1}. \quad (4.16)$$

The truncated non-causal control kernel is defined as

$$\boldsymbol{\Gamma}_{inc}(\tau) = \begin{cases} \boldsymbol{\Gamma}_{nc}(\tau), & \tau \geq 0, \\ 0, & \tau < 0, \end{cases} \quad (4.17)$$

from which the actuation signal is computed as

$$\mathbf{a}_{inc}(t) = \int_{-\infty}^0 \boldsymbol{\Gamma}_{inc}(t - \tau) \mathbf{y}_f(\tau) d\tau. \quad (4.18)$$

As before, truncating the optimal non-causal kernel yields a non-optimal causal kernel.

Finally, the optimal causal controller is

$$\mathbf{a}_c(t) = \int_{-\infty}^0 \boldsymbol{\Gamma}_c(t - \tau) \mathbf{y}_f(\tau) d\tau, \quad (4.19)$$

and the optimal causal control kernel is obtained by using Lagrange multipliers to enforce causality, expressed by the cost function

$$J_c = \int_{-\infty}^{\infty} \mathbb{E}\{\mathbf{z}(t)^\dagger \mathbf{z}(t) + \mathbf{a}(t)^\dagger \mathbf{P} \mathbf{a}(t) + (\boldsymbol{\Lambda}_-(t) \boldsymbol{\Gamma}_c(t) + \boldsymbol{\Lambda}_-^\dagger(t) \boldsymbol{\Gamma}_c^\dagger(t))\} dt. \quad (4.20)$$

Minimizing (4.20) leads to the Wiener-Hopf problem (B.5) with $\hat{\mathbf{K}} = \mathbf{R}_{za}^\dagger \mathbf{R}_{za} + \hat{\mathbf{P}}$ and $\hat{\mathbf{L}} = -\mathbf{R}_{za}^\dagger$. Using the solution of this Wiener-Hopf problem given in (B.9), the optimal causal resolvent-based control kernel is

$$\begin{aligned} \hat{\mathbf{f}}_c(\omega) = & (\mathbf{R}_{za}^\dagger \mathbf{R}_{za} + \hat{\mathbf{P}})_+^{-1} \left((\mathbf{R}_{za}^\dagger \mathbf{R}_{za} + \hat{\mathbf{P}})_-^{-1} (-\mathbf{R}_{za}^\dagger) \mathbf{R}_{zf} \hat{\mathbf{F}} \mathbf{R}_{yf}^\dagger \right. \\ & \left. (\mathbf{R}_{yf} \hat{\mathbf{F}} \mathbf{R}_{yf}^\dagger + \hat{\mathbf{N}})_-^{-1} \right) (\mathbf{R}_{yf} \hat{\mathbf{F}} \mathbf{R}_{yf}^\dagger + \hat{\mathbf{N}})_+^{-1}. \end{aligned} \quad (4.21)$$

In (4.14), (4.18), and (4.19), the actuation signal is obtained as a convolution between the control kernel and the sensor measurement \mathbf{y}_f for the forcing system (4.2), i.e., the control kernels were derived using a measurement excluding the response of the system (4.3) to actuation. In practice, only the complete measurement $\mathbf{y} = \mathbf{y}_f + \mathbf{y}_a$ is available. Considering the full (combined) linear system (4.1), the final closed-loop controller takes the form

$$\mathbf{a}(t) = \int_{-\infty}^0 \boldsymbol{\Gamma}_{cl}(t - \tau) \mathbf{y}(\tau) d\tau, \quad (4.22)$$

where the final closed-loop kernel is

$$\hat{\mathbf{f}}_{cl} = (\mathbf{I} + \hat{\mathbf{f}} \mathbf{R}_{ya})^{-1} \hat{\mathbf{f}}, \quad (4.23)$$

with $\hat{\mathbf{f}}$ replaced by $\hat{\mathbf{f}}_{inc}$ or $\hat{\mathbf{f}}_c$ for truncated non-causal and optimal causal resolvent-based control, respectively.

5 Computing estimation and control kernels

In this section, we present two approaches to compute resolvent-based estimation and control kernels [Martini et al., 2022]. First, we describe an operator-based approach that allows for efficient implementation of linear simulations without the need for inverting the operator or performing prior model reduction, making it particularly efficient for large-scale problems. Second, we explain a data-driven approach that does not require the construction of the linearized Navier-Stokes operator. Instead, this method utilizes training data from simulations or experiments to build cross-spectral densities, which are then used to compute the components of the estimation and control kernels.

5.1 Operator-based approach

The resolvent operator \mathbf{R} is defined in terms of an inverse, the cost of which scales poorly with the problem dimension n and becomes computationally expensive for large systems. To circumvent this, we employ a time-stepping approach that avoids the inverse operation and instead constructs the necessary modified resolvent operators that appear in the estimation and control kernels by solving linear equations in the time domain [Martini et al., 2020, 2022, Farghadan et al., 2023]. For both cases, the cost of this approach scales linearly with the problem dimension, avoiding the need to reduce the system via a priori model reduction and the associated loss of accuracy. Individual modified resolvent operators such as \mathbf{R}_{za} and \mathbf{R}_{ya} can be obtained using a single-stage run of the direct linear equations. Products of modified resolvent operators (and the forcing CSD) such as $\mathbf{R}_{zf} \hat{\mathbf{F}} \mathbf{R}_{yf}^\dagger$ and $\mathbf{R}_{yf} \hat{\mathbf{F}} \mathbf{R}_{yf}^\dagger$ can be obtained with greater efficiency using two-stage runs of both the adjoint and direct linear equations.

5.1.1 Single-stage run

The operators \mathbf{R}_{z_a} and \mathbf{R}_{y_a} appearing in (4.21) and (4.23), respectively, can be constructed by computing a series of impulse responses of the actuation system (4.3),

$$\frac{d\mathbf{q}_{a,k}}{dt}(t) = \mathbf{A}\mathbf{q}_{a,k}(t) + \mathbf{B}_{a,k}\delta(t), \quad (5.1a)$$

$$\mathbf{y}_{a,k}(t) = \mathbf{C}_y\mathbf{q}_{a,k}(t), \quad (5.1b)$$

$$\mathbf{z}_{a,k}(t) = \mathbf{C}_z\mathbf{q}_{a,k}(t). \quad (5.1c)$$

Here, $\mathbf{y}_{a,k} \in \mathbb{C}^{n_y}$ and $\mathbf{z}_{a,k} \in \mathbb{C}^{n_z}$ are the sensor and target measurement of the direct system forced by an impulse $\delta(t)$ located at k -th actuator, as encoded by the k -th column of the actuation matrix, $\mathbf{B}_{a,k}$. By collecting these data for each actuator $k = 1, \dots, n_a$ and taking a Fourier transform, we obtain

$$\hat{\mathbf{Y}}_a = [\hat{\mathbf{y}}_{a,1} \quad \hat{\mathbf{y}}_{a,2} \quad \dots \quad \hat{\mathbf{y}}_{a,n_a}] = \mathbf{R}_{y_a}, \quad (5.2a)$$

$$\hat{\mathbf{Z}}_a = [\hat{\mathbf{z}}_{a,1} \quad \hat{\mathbf{z}}_{a,2} \quad \dots \quad \hat{\mathbf{z}}_{a,n_a}] = \mathbf{R}_{z_a}, \quad (5.2b)$$

with $\hat{\mathbf{Y}}_a \in \mathbb{C}^{n_y \times n_a}$ and $\hat{\mathbf{Z}}_a \in \mathbb{C}^{n_z \times n_a}$. That is, the Fourier transform of each measurement $\mathbf{y}_{a,k}$ and $\mathbf{z}_{a,k}$ yields a column of the modified resolvent operators \mathbf{R}_{y_a} and \mathbf{R}_{z_a} , respectively.

5.1.2 Two-stage run

While single-stage runs could be used to construct all of the modified resolvent operators in the estimation and control kernels, certain products thereof can be constructed more efficiently using pairs of adjoint and direct runs. The procedure begins with solving the adjoint system

$$-\frac{d\mathbf{q}_{f,i}}{dt}(t) = \mathbf{A}^\dagger\mathbf{q}_{f,i}(t) + \mathbf{C}_{y,i}^\dagger\delta(t), \quad (5.3a)$$

$$\mathbf{s}_i(t) = \mathbf{B}_f^\dagger\mathbf{q}_{f,i}(t), \quad (5.3b)$$

where \mathbf{A}^\dagger is the adjoint linearized Navier-Stokes operator and the subscript i indicates the sensor defined by the i -th row of the sensor measurement matrix \mathbf{C}_y . The output \mathbf{s}_i of the adjoint run is used as a forcing in a corresponding direct run of the forcing system (4.2),

$$\frac{d\mathbf{q}_{f,i}}{dt}(t) = \mathbf{A}\mathbf{q}_{f,i}(t) + \mathbf{B}_f\mathbf{s}_i(t), \quad (5.4a)$$

$$\mathbf{y}_{f,i}(t) = \mathbf{C}_y\mathbf{q}_{f,i}(t) + \mathbf{n}_i(t), \quad (5.4b)$$

$$\mathbf{z}_{f,i}(t) = \mathbf{C}_z\mathbf{q}_{f,i}(t), \quad (5.4c)$$

As in the single-stage run, by collecting each of the final sensor and target measurements and taking a Fourier-transforming, we obtain

$$\hat{\mathbf{Y}}_f = [\hat{\mathbf{y}}_1 \quad \hat{\mathbf{y}}_2 \quad \dots \quad \hat{\mathbf{y}}_{n_y}] = \mathbf{R}_{y_f}\mathbf{R}_{y_f}^\dagger, \quad (5.5a)$$

$$\hat{\mathbf{Z}}_f = [\hat{\mathbf{z}}_1 \quad \hat{\mathbf{z}}_2 \quad \dots \quad \hat{\mathbf{z}}_{n_y}] = \mathbf{R}_{z_f}\mathbf{R}_{y_f}^\dagger, \quad (5.5b)$$

with $\hat{\mathbf{Y}}_f \in \mathbb{C}^{n_y \times n_y}$ and $\hat{\mathbf{Z}}_f \in \mathbb{C}^{n_z \times n_y}$. To account for the nonlinearity of the flow, the colored forcing statistics, $\hat{\mathbf{F}}$, can be incorporated into (5.5) during adjoint and direct simulations, resulting in $\mathbf{R}_{y_f}\hat{\mathbf{F}}\mathbf{R}_{y_f}^\dagger$ and $\mathbf{R}_{z_f}\hat{\mathbf{F}}\mathbf{R}_{y_f}^\dagger$ [Jung, 2024].

Finally, (5.2) and (5.5) are used to write the estimation kernels in (4.8) and (4.13) and control kernels in (4.16) and (4.21) in terms of $\hat{\mathbf{Y}}_a$, $\hat{\mathbf{Z}}_a$, $\hat{\mathbf{Y}}_f$, and $\hat{\mathbf{Z}}_f$. The final operator-based estimation and control kernels are

$$\hat{\mathbf{T}}_{nc,O} = \hat{\mathbf{Z}}_f(\hat{\mathbf{Y}}_f + \hat{\mathbf{N}})^{-1}, \quad (5.6a)$$

$$\hat{\mathbf{T}}_{c,O} = (\hat{\mathbf{Z}}_f(\hat{\mathbf{Y}}_f + \hat{\mathbf{N}})^{-1})_+(\hat{\mathbf{Y}}_f + \hat{\mathbf{N}})^{-1}_+, \quad (5.6b)$$

and

$$\hat{\mathbf{F}}_{nc,O} = (\hat{\mathbf{Z}}_a^\dagger \hat{\mathbf{Z}}_a + \hat{\mathbf{P}})^{-1}(-\hat{\mathbf{Z}}_a^\dagger) \hat{\mathbf{Z}}_f(\hat{\mathbf{Y}}_f + \hat{\mathbf{N}})^{-1}, \quad (5.7a)$$

$$\hat{\mathbf{F}}_{c,O} = (\hat{\mathbf{Z}}_a^\dagger \hat{\mathbf{Z}}_a + \hat{\mathbf{P}})^{-1}_+ \left((\hat{\mathbf{Z}}_a^\dagger \hat{\mathbf{Z}}_a + \hat{\mathbf{P}})^{-1}(-\hat{\mathbf{Z}}_a^\dagger) \hat{\mathbf{Z}}_f(\hat{\mathbf{Y}}_f + \hat{\mathbf{N}})^{-1} \right)_+ (\hat{\mathbf{Y}}_f + \hat{\mathbf{N}})^{-1}_+. \quad (5.7b)$$

5.2 Data-driven approach

When the linearized Navier-Stokes operator is unavailable, a data-driven approach [Martini et al., 2022] can be employed to build the required modified resolvent operators using CSDs computed from data [Towne et al., 2018, 2020]. This approach extends the applicability of resolvent-based estimation and control to experimental settings and circumvents the need for adjoint solvers. Additionally, when the CSD is computed from the dataset of a nonlinear system, the resulting kernels automatically include the forcing CSD $\hat{\mathbf{F}}$, which statistically accounts for the nonlinearity of the flow, thereby improving the estimation and control performance for the nonlinear system.

The nonlinear terms in the Navier-Stokes equations act as a forcing of the resolvent operator [McKeon and Sharma, 2010], and their influence is crucial in complex dynamic systems [Amaral et al., 2021]. To explicitly address the nonlinear terms, we split the forcing vector \mathbf{f} into two components: the external forcing \mathbf{f}_{ext} and the nonlinear terms \mathbf{f}_{nl} . This distinction helps us better understand their impact when building the CSDs from the data. The overall forcing term in (4.1) can be split as

$$\mathbf{B}_f \mathbf{f} = \begin{bmatrix} \mathbf{B}_{ext} & \mathbf{B}_{nl} \end{bmatrix} \begin{bmatrix} \mathbf{f}_{ext} \\ \mathbf{f}_{nl} \end{bmatrix} \quad (5.8)$$

where $\mathbf{B}_{ext} \in \mathbb{C}^{n \times n_{ext}}$ and $\mathbf{B}_{nl} \in \mathbb{C}^{n \times n}$. Typically, the region subject to external forcing is smaller than the overall domain, such that $n_{ext} < n$. In a linear system, the nonlinear terms \mathbf{f}_{nl} are not included, allowing us to analyze the linear dynamics of the flow and to build linear estimators and controllers. However, our ultimate goal is to manipulate the unsteady fluctuations inherent in the actual flow, which necessitates considering nonlinearity. For the nonlinear system, we collect data from the systems without and with external forcing to better capture the behavior of the systems influenced by external forcing. The forcing system (4.2) without and with the external forcing can be expressed as

$$\frac{d\mathbf{q}}{dt}(t) = \mathbf{A}\mathbf{q}(t) + \mathbf{B}_{nl}\mathbf{f}_{nl}(t), \quad (5.9)$$

$$\frac{d\mathbf{q}_e}{dt}(t) = \mathbf{A}\mathbf{q}_e(t) + \mathbf{B}_{ext}\mathbf{f}_{ext} + \mathbf{B}_{nl}\mathbf{f}_{nl,e}(t). \quad (5.10)$$

The subscript e indicates the flow quantity that contains the development of nonlinearity, which was impacted by the external forcing. The $\mathbf{f}_{nl,e}$ term is evolved by the external forcing in time and space, so in the nonlinear system, the nonlinear effect can not be neglected. Equation (5.9) is the DNS or LES system without any source term. We assume external and nonlinear forcings are uncorrelated. Then we obtain

$$\begin{bmatrix} \hat{\mathbf{y}}_{f,nl} \\ \hat{\mathbf{z}}_{f,nl} \end{bmatrix} = \begin{bmatrix} \mathbf{R}_{yf,nl} \\ \mathbf{R}_{zf,nl} \end{bmatrix} \hat{\mathbf{f}}_{nl} + \begin{bmatrix} \hat{\mathbf{n}} \\ 0 \end{bmatrix}, \quad (5.11)$$

$$\begin{bmatrix} \hat{\mathbf{y}}_{f,ext,nl} \\ \hat{\mathbf{z}}_{f,ext,nl} \end{bmatrix} = \begin{bmatrix} \mathbf{R}_{yf,ext} & \mathbf{R}_{yf,nl} \\ \mathbf{R}_{zf,ext} & \mathbf{R}_{zf,nl} \end{bmatrix} \begin{bmatrix} \hat{\mathbf{f}}_{ext} \\ \hat{\mathbf{f}}_{nl,e} \end{bmatrix} + \begin{bmatrix} \hat{\mathbf{n}} \\ 0 \end{bmatrix}. \quad (5.12)$$

Computing the cross-spectral density of $[\hat{\mathbf{y}} \quad \hat{\mathbf{z}}]^T$ from (5.11) and (5.12) gives

$$\begin{bmatrix} \mathbf{S}_{yy} \\ \mathbf{S}_{zy} \end{bmatrix} \triangleq \begin{bmatrix} \mathbf{S}_{yy,f,nl} \\ \mathbf{S}_{zy,f,nl} \end{bmatrix} = \begin{bmatrix} \mathbf{R}_{yf,nl} \hat{\mathbf{F}}_{nl} \mathbf{R}_{yf,nl}^\dagger + \hat{\mathbf{N}} \\ \mathbf{R}_{zf,nl} \hat{\mathbf{F}}_{nl} \mathbf{R}_{yf,nl}^\dagger \end{bmatrix}, \quad (5.13)$$

$$\begin{bmatrix} \mathbf{S}_{yy,e} \\ \mathbf{S}_{zy,e} \end{bmatrix} \triangleq \begin{bmatrix} \mathbf{S}_{yy,f,ext,nl} \\ \mathbf{S}_{zy,f,ext,nl} \end{bmatrix} = \begin{bmatrix} \mathbf{R}_{yf,nl} \hat{\mathbf{F}}_{nl,r} \mathbf{R}_{yf,nl}^\dagger + \mathbf{R}_{yf,ext} \hat{\mathbf{F}}_{ext} \mathbf{R}_{yf,ext}^\dagger + \hat{\mathbf{N}} \\ \mathbf{R}_{zf,nl} \hat{\mathbf{F}}_{nl,r} \mathbf{R}_{yf,nl}^\dagger + \mathbf{R}_{zf,ext} \hat{\mathbf{F}}_{ext} \mathbf{R}_{yf,ext}^\dagger \end{bmatrix}. \quad (5.14)$$

with $\mathbf{S}_{yy} = \mathbb{E}\{\hat{\mathbf{y}}\hat{\mathbf{y}}^\dagger\}$ and $\mathbf{S}_{zy} = \mathbb{E}\{\hat{\mathbf{z}}\hat{\mathbf{y}}^\dagger\}$. Since the right-hand sides of (5.13) and (5.14) contain the terms needed to build the estimation and control kernels (4.8), (4.13), (4.16), and (4.21), this shows that the CSDs on the left-hand side can be used in their place. Note that the CSDs inherently contain statistical information about the nonlinearity of the flow within the forcing CSD matrix.

The data-driven non-causal and causal estimation kernels in (4.8) and (4.13) are computed using the CSDs from (5.13), yielding

$$\hat{\mathbf{T}}_{nc,D} = \mathbf{S}_{zy} (\mathbf{S}_{yy} + \hat{\mathbf{N}})^{-1}, \quad (5.15a)$$

$$\hat{\mathbf{T}}_{c,D} = (\mathbf{S}_{zy} (\mathbf{S}_{yy} + \hat{\mathbf{N}})^{-1})_+ (\mathbf{S}_{yy} + \hat{\mathbf{N}})_+^{-1}. \quad (5.15b)$$

The control kernels require \mathbf{R}_{ya} and \mathbf{R}_{za} , which do not include the forcing CSD matrix and can be obtained by imposing an impulse forcing at the actuator location in the nonlinear system,

$$\frac{d\mathbf{q}_{a,k}}{dt}(t) = \mathbf{A}\mathbf{q}_{a,k}(t) + \mathbf{B}_{a,k}\delta(t) + \mathbf{B}_{nl}\mathbf{f}_{nl,k}(t). \quad (5.16)$$

The Fourier-transformed sensor and target reading from the nonlinear system forced by impulses at the actuator locations are subtracted by the same quantities, $\hat{\mathbf{y}}_{f,nl}$ and $\hat{\mathbf{z}}_{f,nl}$, from the nonlinear system without the actuators. Then we obtain

$$\begin{bmatrix} \hat{\mathbf{Y}}_s \\ \hat{\mathbf{Z}}_s \end{bmatrix} = \begin{bmatrix} \hat{\mathbf{y}}_a - \hat{\mathbf{y}}_{f,nl} \\ \hat{\mathbf{z}}_a - \hat{\mathbf{z}}_{f,nl} \end{bmatrix} \approx \begin{bmatrix} \mathbf{R}_{ya} \\ \mathbf{R}_{za} \end{bmatrix}, \quad (5.17)$$

where the subscript s denotes the Fourier-transformed readings computed through subtraction using the data-driven approach. The resulting CSDs are

$$\begin{bmatrix} \mathbf{S}_{yy,s} \\ \mathbf{S}_{zz,s} \end{bmatrix} = \begin{bmatrix} \mathbf{R}_{ya} \mathbf{R}_{ya}^\dagger \\ \mathbf{R}_{za} \mathbf{R}_{za}^\dagger \end{bmatrix} \approx \begin{bmatrix} \mathbf{Y}_a \mathbf{Y}_a^\dagger \\ \mathbf{Z}_a \mathbf{Z}_a^\dagger \end{bmatrix}. \quad (5.18)$$

Using this result, we can finally obtain the data-driven control kernels,

$$\hat{\mathbf{T}}_{nc,D} = (\mathbf{S}_{zz,s}^\dagger + \hat{\mathbf{P}})^{-1} (-\hat{\mathbf{Z}}_s^\dagger) \mathbf{S}_{zy} (\mathbf{S}_{yy} + \hat{\mathbf{N}})^{-1}, \quad (5.19a)$$

$$\hat{\mathbf{T}}_{c,D} = (\mathbf{S}_{zz,s}^\dagger + \hat{\mathbf{P}})_+^{-1} \left((\mathbf{S}_{zz,s}^\dagger + \hat{\mathbf{P}})^{-1} (-\hat{\mathbf{Z}}_s^\dagger) \mathbf{S}_{zy} (\mathbf{S}_{yy} + \hat{\mathbf{N}})^{-1} \right)_+ (\mathbf{S}_{yy} + \hat{\mathbf{N}})_+^{-1}. \quad (5.19b)$$

To apply these kernels to the system that is excited by the external forcing, \mathbf{S}_{yy} and \mathbf{S}_{zy} can be replaced with $\mathbf{S}_{yy,r}$ and $\mathbf{S}_{zy,r}$.

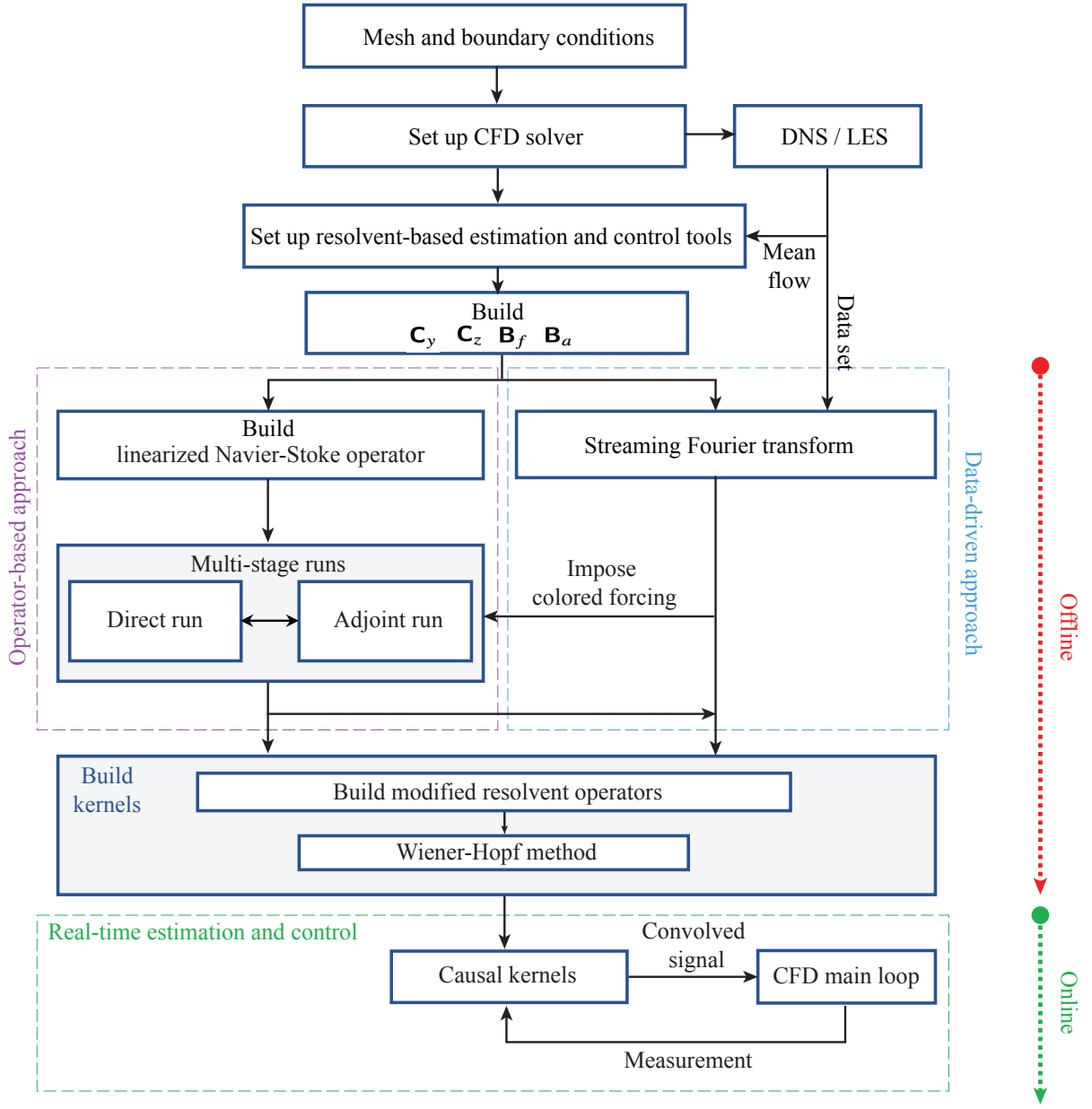


FIGURE 7: Flow chart for the new implementation of resolvent-based estimation and control tools within the compressible flow solver CharLES.

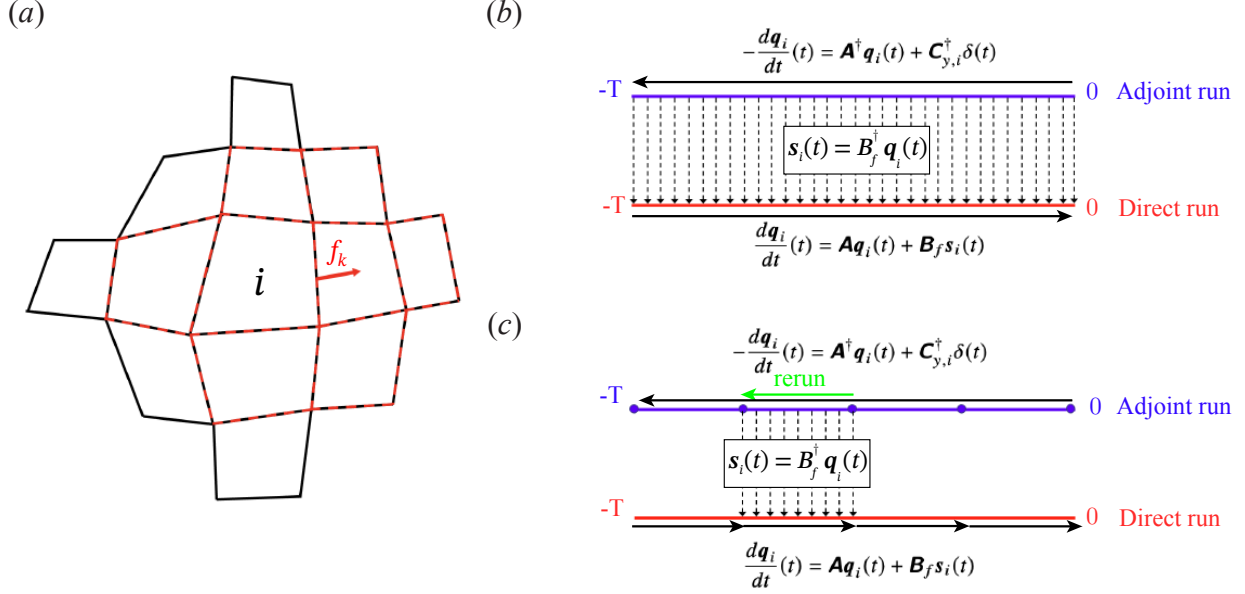


FIGURE 8: Linearization within the CharLES solver: (a) The computational stencil for a control volume (CV_{*i*}) labeled *i*. The computational stencil needed to compute the flux at a specific face *k* of CV_{*i*} is shown with red dashed lines. The CV-based stencil is the union of all face-based stencils for a given CV. A schematic of the two-stage adjoint-direct run: (b) without checkpointing and (c) with checkpointing. Checkpoints are marked with solid blue circles.

6 Implementation of a resolvent-based estimation and control tool

In this section, we describe our implementation of the resolvent-based estimation and control tools described in §4 and §5 within CharLES, an unstructured compressible flow solver for large-scale problems within a high-performance computing environment. The conceptual flow chart for the software is depicted in figure 7. These tools can be used for any flows simulated within the CharLES solver [Brès et al., 2017] and can be linked with any external packages written in C/C++. To parallelize linear algebra computation and streaming Fourier transform, we integrated the solver with PETSc [Balay et al., 2019] and FFTW [Frigo and Johnson, 2005].

6.1 Linearization

The operator-based approach in §5 requires access to the linear operator \mathbf{A} or the actions of both the linear and adjoint operators. We use a matrix-forming approach in which the linear operator is directly computed and stored within the nonlinear solver. This approach accounts for the numerical schemes and boundary conditions employed in the nonlinear simulations and ensures that the linear operator is readily available at run-time. Extracting the linear operator from large-scale, compressible CFD solvers is not a trivial task, and several approaches have been suggested in the literature [Nielsen and Kleb, 2006, Fosas et al., 2012, Cook et al., 2018, Bhagwat, 2020]. The approach we adopt most closely mirrors that of Nielsen and Kleb [2006] and Cook et al. [2018].

The CharLES solver uses a control-volume-based finite volume method. A straightforward way to extract the linear operator numerically is to use a finite-difference approximation of the Jacobian, computing the linear operator one column at a time. For example, the j^{th} column of the linear operator can be extracted

using a second-order approximation as

$$\mathbf{A}(:, j) = \frac{\mathcal{F}(\bar{\mathbf{q}} + \epsilon \mathbf{e}_j) - \mathcal{F}(\bar{\mathbf{q}} - \epsilon \mathbf{e}_j)}{2\epsilon}, \quad (6.1)$$

where j refers to the j -th degree of freedom and \mathcal{F} represents the right-hand-side of CFD code (the discretized nonlinear compressible Navier-Stokes operator). However, this approach is computationally expensive, as the number of the global right-hand-side evaluations (\mathcal{F}) required to form the operator equals the problem dimension n .

Instead, we use an approach adopted by [Nielsen and Kleb \[2006\]](#) and more recently applied by [Cook et al. \[2018\]](#) that relies on perturbing multiple degrees of freedom (DOF) simultaneously. The key insight is that perturbing an element of the state vector \mathbf{q} affects only a small number of nearby control volumes, known as its computational stencil. This stencil is determined by the numerics used in the Charles solver [[Brès et al., 2017](#)]. Thus, it is feasible to perturb multiple elements of the state vector at once without the perturbations interfering with each other. This approach allows us to compute multiple columns of \mathbf{A} simultaneously, significantly reducing the computational cost. This is accomplished by replacing unit vector \mathbf{e}_j in (6.1) with $\tilde{\mathbf{e}}_k$, which represents the multiple degrees of freedom perturbed simultaneously. Using this approach, the number of right-hand-side evaluations $\mathcal{F}(\mathbf{q})$ scales with the extent of the computational stencil, not with the size of the problem. In the spatial discretization in CharLES, the flux at a face depends on the adjoining control volumes and their immediate face neighbors, as illustrated in figure 8(a).

To optimize the process of building the $\tilde{\mathbf{e}}_k$ vectors, we sort the computational grid into lists of non-overlapping degrees of freedom on a single processor and then broadcast this information to all other processors. The linearized compressible Navier-Stokes operator \mathbf{A} is extracted and saved at the initial step, and the routine is performed only once before the time-stepping or nonlinear runs (DNS or LES). Typically, the number of right-hand-side evaluations required for standard hexahedral/quadrilateral grids is approximately 125 and 300 for 2D and 3D problems, respectively. The small parameter ϵ in (6.1) is empirically chosen to minimize the error in the numerical derivatives. We have found $\epsilon = \epsilon_0 \|\mathbf{q}\|$ with $\epsilon_0 = 10^{-6}$ to be an effective and robust choice. The $\|\mathbf{q}\|$ is computed separately for each quantity (density, velocities, and energy).

6.2 Efficient implementation of the estimation and control tools

To effectively store and utilize the linear operator for large-scale numerical linear algebra computations such as matrix-vector products, we parallelize our implementation using the open-source linear algebra package PETSc [[Balay et al., 2019](#)]. PETSc leverages the underlying domain decomposition used by the CFD solver to partition the computational grid. Once the matrices such as \mathbf{A} , \mathbf{C}_y , \mathbf{C}_z , \mathbf{B}_a , and \mathbf{B}_f are constructed, PETSc is used to advance the linear dynamics for the single or two-stage runs described in §5.1. To advance these equations in time, we use the TVD-RK3 scheme [[Gottlieb and Shu, 1998](#)], the same scheme used by the nonlinear solver.

In the two-stage run described in §5.1.2, the time-series data of $s_i(t)$ from (5.3b) must be stored to serve as the forcing term $\mathbf{B}_f s_i(t)$ in (5.4a), as shown schematically in figure 8(b). However, storing all snapshots from the initial step of the adjoint run to the time T where the direct run begins becomes prohibitively expensive over long time horizons. We use checkpointing, as shown in figures 8(c), to address this issue by only storing snapshots at particular intervals during the adjoint run in (5.3a). After completing the first full adjoint run, the direct run is advanced in chunks. The adjoint run is then rerun between the last two checkpoints, using only the stored snapshots within that interval, before conducting the direct run through the same interval. This approach reduces memory usage, which is particularly beneficial for large-scale problems. For example, if advancing N_t timesteps in the adjoint run, the storage requirement can be reduced from $O(N_t)$ to $O(W_t + N_t/W_t)$, where W_t is the length of the interval between two checkpoints, and

N_t/W_t roughly indicates the number of checkpoints. The minimum memory requirement is achieved when $W_t \approx \sqrt{N_t}$. Thus, checkpointing reduces the memory required from $O(N_t)$ to $O(2\sqrt{N_t})$.

Constructing the data-driven estimation and control kernels (5.15) and (5.19) requires the computation of CSDs, as described in §5.2. Typically, CSDs are computed using FFTs, which require simultaneous access to many snapshots of the state (to be precise, the number of desired frequencies n_{freq}). However, this approach quickly becomes infeasible when each snapshot is large, i.e., when the state dimension n is large. To reduce data size and memory usage, we employ streaming discrete Fourier transforms (DFTs), as proposed by Schmidt and Towne [2019] within the context of a streaming algorithm for spectral proper orthogonal decomposition (SPOD) and further utilized by Farghadan et al. [2023] within a scalable time-stepping algorithm for resolvent analysis.

The streaming algorithm requires access to only one instantaneous snapshot of the state at a time, avoiding the need to store the entire time-series. This is achieved by using the definition of the discrete Fourier transform (DFT), which yields results equivalent to the FFT. Each snapshot contributes to the summation of the Fourier modes as

$$\hat{\mathbf{f}}_k^l = \sum_{j=1}^{n_{freq}} \mathbf{f}_j^l p_{jk}, \quad (6.2)$$

where $p_{jk} = e^{(k-1)(j-1)(-i2\pi/n_{freq})}$, with k representing the k -th frequency, j the j -th snapshot, and l the l -th block of data. The full time series data is divided into multiple blocks, each windowed with a 50% overlap. Each snapshot is multiplied by the complex scalar p_{jk} and added to the summation of the Fourier modes. Our implementation is integrated with FFTW [Frigo and Johnson, 2005] and stores the DFT matrix $\mathbb{C}^{n_{freq} \times n_{freq}}$ during the initialization step of the CFD solver.

6.3 Extracting nonlinear terms

Extracting the nonlinear terms (\mathbf{f}_{nl} in (5.8)) of Navier-Stokes equations is useful to investigate the nonlinear interactions. The nonlinear terms are extracted within the application developed for the resolvent-based estimation and control tool. The principle is described here.

The nonlinear Navier-Stokes operator \mathcal{F} can be expressed as

$$\mathcal{F}(\mathbf{q}) = \mathcal{F}(\bar{\mathbf{q}}) + \frac{\partial \mathcal{F}(\bar{\mathbf{q}})}{\partial \mathbf{q}} \mathbf{q}' + nl(\mathbf{q}'), \quad (6.3)$$

where $nl(\mathbf{q}')$ represents all remaining nonlinear terms after linearization. The forcing vector that accounts for the nonlinear terms can be derived as follows

$$\mathbf{f}_{nl}(\mathbf{q}') = \mathcal{F}(\bar{\mathbf{q}}) + nl(\mathbf{q}') = \underbrace{\mathcal{F}(\mathbf{q})}_{\text{from DNS}} - \underbrace{\mathbf{A}\mathbf{q}'}_{\text{from linear run}}. \quad (6.4)$$

We run the nonlinear simulation (DNS or LES) in time and, within the same loop, compute the term $\mathbf{A}\mathbf{q}'$ to subtract from $\mathcal{F}(\mathbf{q})$. The resulting nonlinear term \mathbf{f}_{nl} is saved in the solver. Computing the CSDs of the nonlinear term requires significant memory due to the large n_{nl} . Therefore, to efficiently compute $\hat{\mathbf{F}}$, we utilize a streaming Fourier transform in (6.2), which doesn't require to save all the snapshot \mathbf{f}_{nl} .

7 Resolvent-based estimation results

In this section, we use the resolvent-based estimation framework to estimate velocity fluctuations in the wake of the airfoil. We expect this framework to be well-suited for this task since the flow is globally stable and resolvent modes capture the vortex shedding, as demonstrated in figures 4 and 5, respectively.

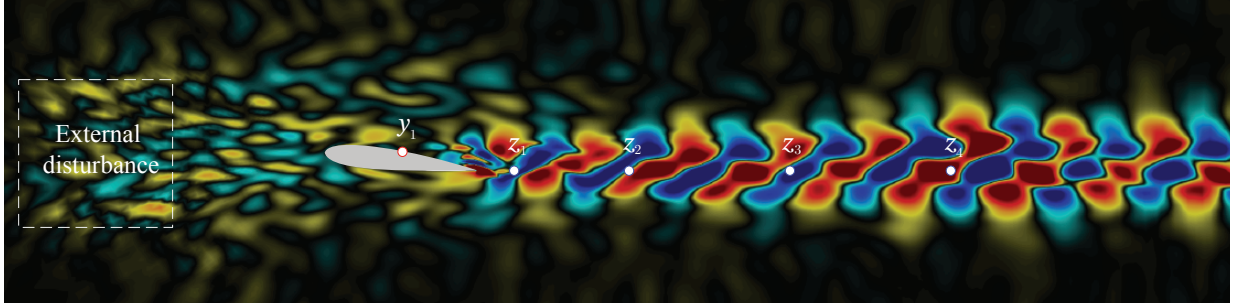


FIGURE 9: Estimation set up for the linear system, showing the locations of the upstream forcing (white box), sensors (red circle), and targets (blue circle). The contours show an instantaneous snapshot of the streamwise velocity fluctuation.

Before considering the actual nonlinear flow of interest, we first evaluate the performance of the resolvent-based estimator applied to the linear system (excited by upstream disturbances) on which the estimator is based. We then turn our attention to the true, nonlinear system with clean and noisy freestream conditions. As discussed previously, the noisy freestream prevents the flow from falling into a periodic limit cycle, resulting in chaotic fluctuations in the wake.

The measurements \mathbf{y} used by the estimator correspond to one or more shear stress sensors on the surface of the airfoil, extracted from the state \mathbf{q} by an appropriately defined measurement matrix \mathbf{C}_y . To mimic the effect of sensors of finite size and to facilitate convergence on a finite grid, the sensors and targets have Gaussian spatial support of the form

$$\alpha e^{-(x-x_c)^2/2\sigma_x^2 - (y-y_c)^2/2\sigma_y^2}, \quad (7.1)$$

where σ_x and σ_y set the width of the Gaussian function and the constant α is set so that the kernel integrates to one.

7.1 Linear system

Figure 9 shows an instantaneous snapshot of the streamwise velocity fluctuation for the linear system driven by an external disturbance in the upstream region. The dominant wake mode, closely resembling the least stable eigenmode and the optimal resolvent response mode, is clearly visible.

7.1.1 Building estimation kernels with white noise forcing

We begin by demonstrating how to construct the estimation kernel using the operator-based approach described in §5.1. A sensor (y_1) is placed on the suction surface of the airfoil at $x/L_c = 0.5$, and four targets (z_1, z_2, z_3, z_4) are positioned in the wake aligned with the trailing edge at $x/L_c = [1.2, 2.0, 3.0, 4.0]$ and $y/L_c = -0.11$, as illustrated in figure 9. In figure 10, we show an example of the two-stage run used to build the operator-based kernel between sensor y_1 and targets z_1 or z_2 . An impulsive forcing is applied to the adjoint system at the sensor location at time zero, as shown in figure 10(a). This forcing has Gaussian temporal and spatial support, with $\sigma_t = 12.5$ and $\sigma_x = \sigma_y = 0.02$, and the sensors and targets have the same spatial support. The input matrix \mathbf{B}_f is defined such that the external forcing \mathbf{f}_{ext} is defined only in the prescribed upstream region. The forcing CSD matrix is assumed to be white noise, i.e., $\mathbf{F}_{ext} = \mathbf{I}$, implying that the forcing is uncorrelated in space and time. The sensor noise CSD is $\hat{\mathbf{N}} = \epsilon \mathbf{I}$, with ϵ equal to 0.1 of

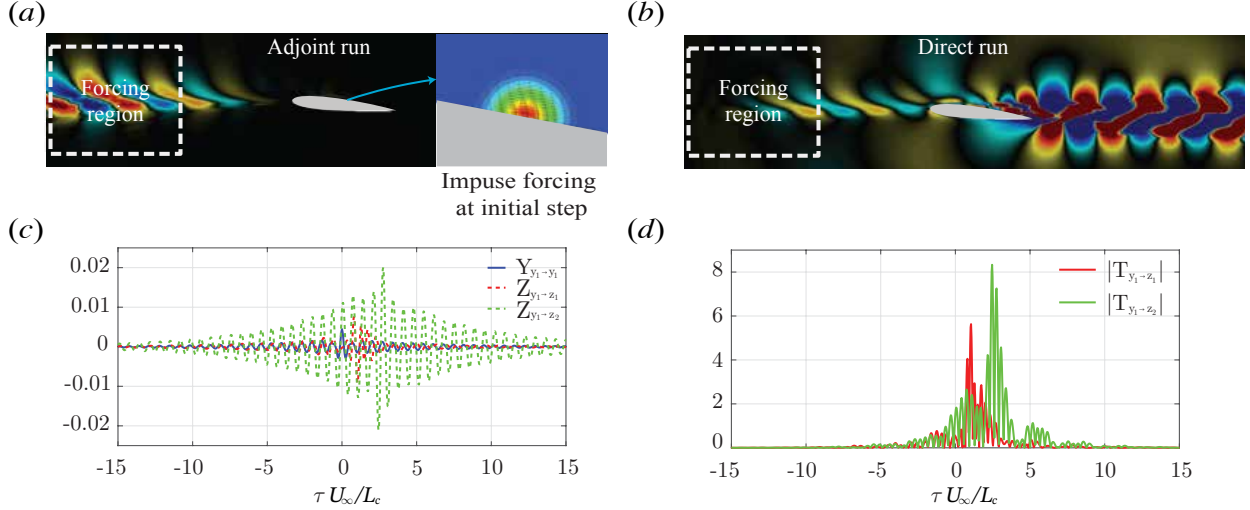


FIGURE 10: Operator-based estimation approach: (a) Snapshot of the adjoint run at a specific time instant, including a zoom-in of the impulsive forcing applied at time zero; (b) Snapshot of the direct run forced by the \mathbf{B}_f readings from the adjoint run; (c) sensor and target readings y_1 [$x/L_c = 0.5$], z_1 [$x/L_c = 1.2$], and z_2 [$x/L_c = 2.0$] from the direct run in (b); (d) Non-causal estimation kernels constructed using the readings from (c).

the maximum value of $\hat{\mathbf{Y}}$. While sensor noise amplitude can affect the smoothness of the estimated data, it does not significantly impact its amplitude or phase.

The readings s_i from the adjoint run are then used to force the direct run, leading to the response shown in figure 10(b). The corresponding sensor and target measurements are recorded in \mathbf{Y} and \mathbf{Z} , as defined in (5.5) and shown in 10(c). \mathbf{Y} is symmetric about $\tau U_\infty / L_c = 0$ as it is autocorrelation. The perturbation grows as it travels downstream, so $Z_{y_1 \rightarrow z_2}$ is generally greater than $Z_{y_1 \rightarrow z_1}$. To achieve convergence in the adjoint and direct runs, we simulate the two-stage run over a time span $tU_\infty / L_c \in [-36, 36]$ with a time step twice that of the DNS.

The Fourier-transformed data, $\hat{\mathbf{Y}}$ and $\hat{\mathbf{Z}}$, are equivalent to $\mathbf{R}_{y_f} \mathbf{R}_{y_f}^\dagger$ and $\mathbf{R}_{z_f} \mathbf{R}_{y_f}^\dagger$, as shown in (5.5). Finally, the Fourier-transformed data are used to form the resolvent-based kernels using (5.6). Figure 10(d) illustrates the estimation kernel \mathbf{T}_{nc} in (4.8) computed from \mathbf{Y} and \mathbf{Z} . The peaks of $T_{y_1 \rightarrow z_1}$ and $T_{y_1 \rightarrow z_2}$ can be explained as the travel time from the sensor location (where the impulse forcing is imposed) to the target. A second dominant peak is observed for $T_{y_1 \rightarrow z_1}$ and $T_{y_1 \rightarrow z_2}$ on the left side of the main peaks, which may be the result of acoustic waves, which are faster than the hydrodynamic waves. For the estimation kernels, $\tau U_\infty / L_c > 0$ and $\tau U_\infty / L_c < 0$ represent past and future times, respectively. Both kernels shown in figure 10(d) have non-zero amplitude mainly for $\tau U_\infty / L_c > 0$, i.e., they are nearly causal. If a significant non-causal part is present, truncating it will degrade the performance of the estimator; optimality, under the constraint of causality, can be restored using the Wiener-Hopf decomposition. This impact is more significant for the nonlinear system, so we will discuss it in greater detail in that section.

7.1.2 Estimation results for the linear system

We present the causal resolvent-based estimation result only using a single sensor, comparing the true streamwise velocity fluctuation u'_x with the estimated value over time. Additionally, we estimate the fluctuations of both the streamwise u'_x and cross-streamwise u'_y velocity components in an extended region

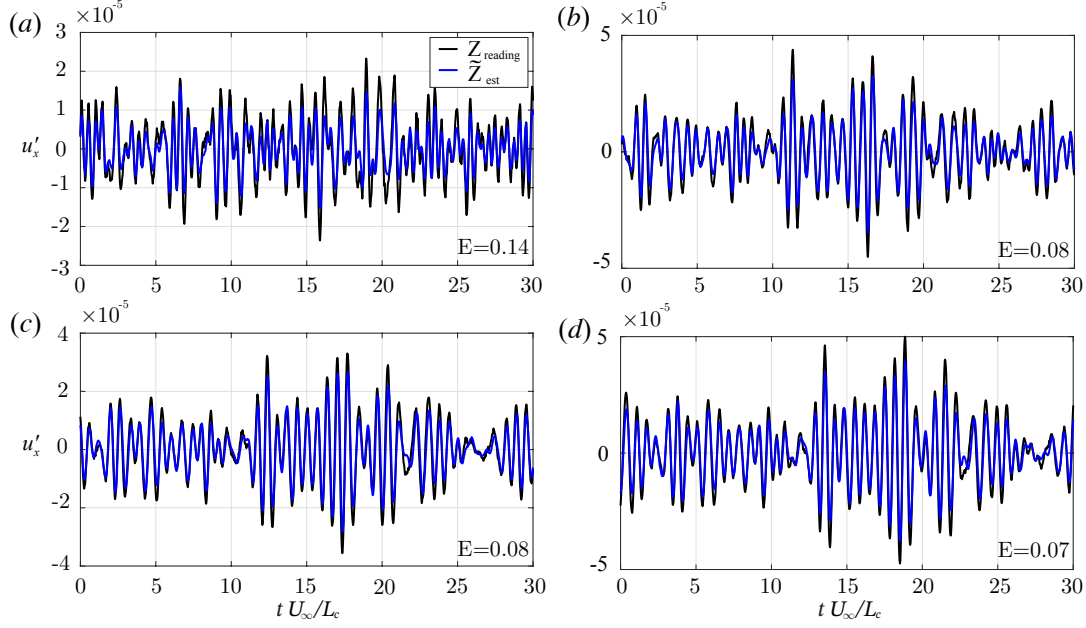


FIGURE 11: Causal estimation using an operator-based approach for the linear system at the targets: (a) z_1 , (b) z_2 , (c) z_3 , and (d) z_4 at positions $[x/L_c = 1.2, 2.0, 3.0, 4.0]$, as shown in Figure 9. The estimation error (7.2) is reported for each case.

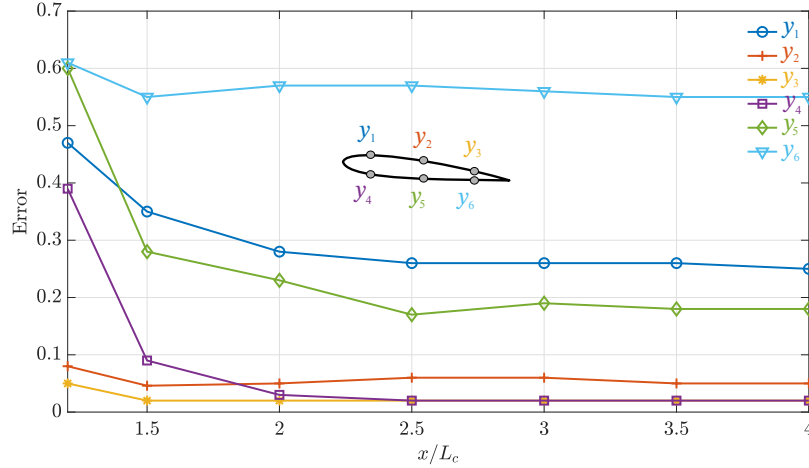


FIGURE 12: Estimation error for the linear system as a function of the target location x/L_c and $y/L_c = 0$.

of the targets using a small number of sensors. To quantify the accuracy of the estimates, we calculate the estimation error

$$E = \frac{\sum_i \int (\tilde{z}_i(t) - z_i(t))^2 dt}{\sum_i \int (z_i(t))^2 dt}, \quad (7.2)$$

where \tilde{z}_i and z_i represent the estimated and true values for the i -th target, respectively. In computing the estimation error, we assume the system is ergodic, allowing the ensemble average to be replaced by the time average.

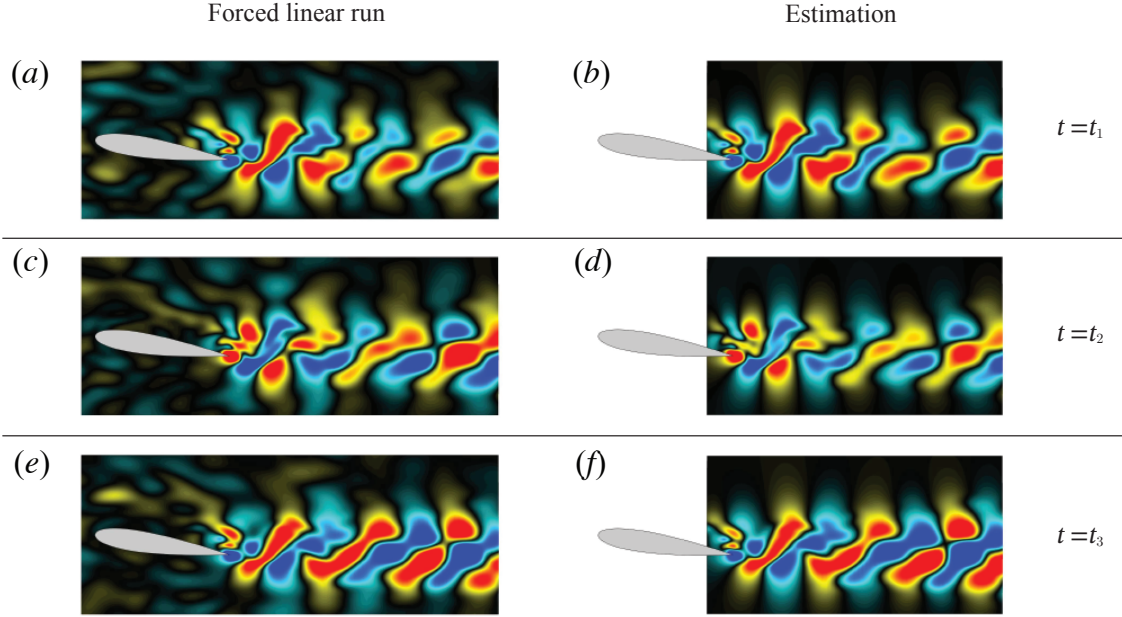


FIGURE 13: Estimation of streamwise velocity fluctuation for the extended target region at three different time steps for the linear system using the sensor y_3 , as shown in figure 12.

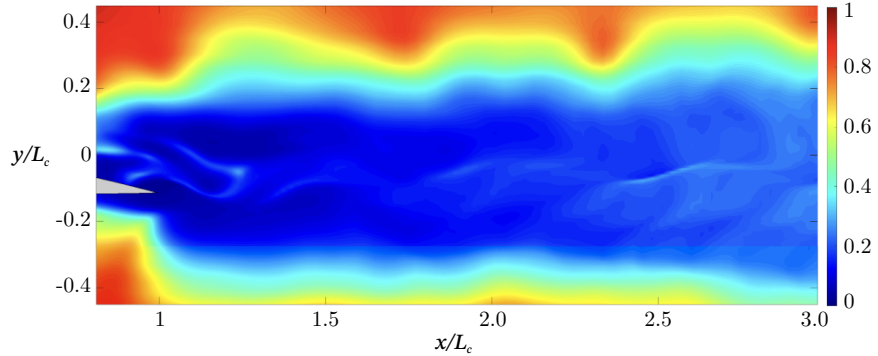


FIGURE 14: Estimation error in the extended target regions for the linear system using the sensor y_3 .

Since the estimator was designed for this linear system, the causal estimates are theoretically optimal. Figure 11 shows examples of the true and estimated target readings as a function of time. The result indicates that the target near the trailing edge, positioned in a more complex flow region, is estimated less accurately. In contrast, the other three targets (z_2 , z_3 , and z_4) show better estimation with an error of 0.07–0.08. Overall, the frequency and amplitude of the fluctuations are well estimated.

Next, we explore the impact of the sensor location on the estimation accuracy. Figure 12 shows the estimation error as a function of the target location x/L_c (aligned with the trailing edge) for six different sensor locations on the airfoil surface. For targets near the trailing edge ($x/L_c < 1.5$), the front sensors on the suction side (y_1) and pressure side (y_6) produce inaccurate estimates. In contrast, the rear sensors (y_3 and y_4) and the middle sensor y_2 , which is the location used to demonstrate building the kernels in the previous section, result in better estimation accuracy. The suction-side sensors y_2 and y_3 accurately capture

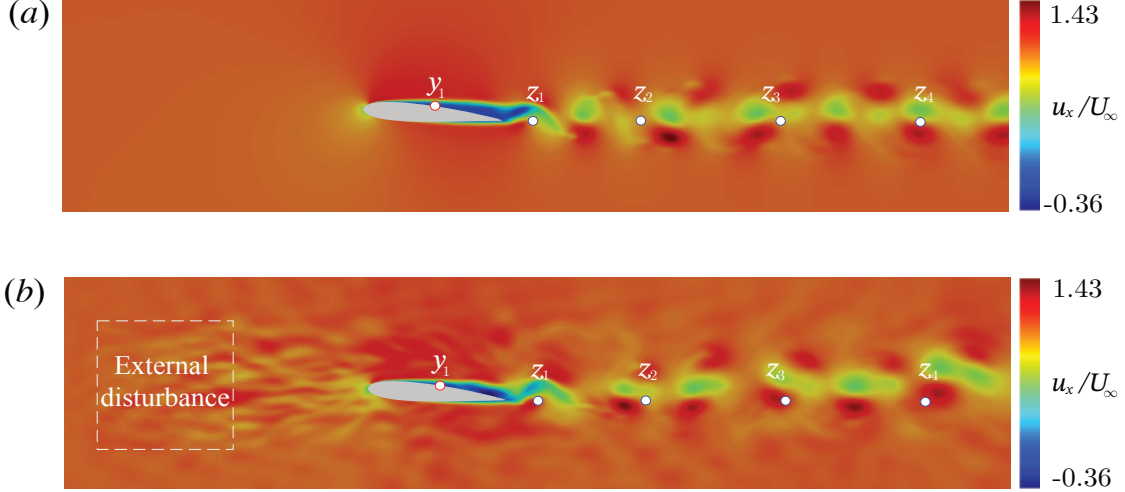


FIGURE 15: Instantaneous snapshot of the streamwise velocity u_x for (a) the clean and (b) the noisy DNS cases. The symbols show the sensor and target locations. The noisy freestream is generated by a random forcing within the region $x/L_c \in [-2, -1]$ and $y/L_c \in [-0.5, 0.5]$.

the flow dynamics near the trailing edge generated by the separation bubble over the airfoil. While y_4 faces challenges in capturing flow information from the bottom of the airfoil, it can still estimate the downstream targets ($x/L_c > 2$) as effectively as the sensors y_2 and y_3 .

Finally, we estimate the state in an extended region of the flow rather than at individual, discrete targets, allowing us to evaluate the estimation accuracy in different regions. The estimation kernel in this context takes the form

$$\begin{bmatrix} \hat{z}_1 \\ \hat{z}_2 \\ \vdots \\ \hat{z}_{n_z} \end{bmatrix} = \begin{bmatrix} \hat{T}_{z_1 y_1} & \hat{T}_{z_1 y_2} & \cdots & \hat{T}_{z_1 n_y} \\ \hat{T}_{z_2 y_1} & \hat{T}_{z_2 y_2} & \cdots & \hat{T}_{z_2 n_y} \\ \vdots & \vdots & \ddots & \vdots \\ \hat{T}_{z_{n_z} y_1} & \hat{T}_{z_{n_z} y_2} & \cdots & \hat{T}_{z_{n_z} n_y} \end{bmatrix} \begin{bmatrix} \hat{y}_1 \\ \hat{y}_2 \\ \vdots \\ \hat{y}_{n_y} \end{bmatrix} \quad (7.3)$$

where n_y and n_z represent the number of sensors and targets, respectively. Based on the optimal results from figure 12, we use just one sensor located on the suction side, y_3 . Figure 13 shows snapshots of the estimates in the extended target regions. The three time steps t_1, t_2, t_3 are selected to represent different phases of the vortex shedding. Figure 14 shows the estimation error as a function of position within the extended target region. As expected, the error increases as the target moves downstream or laterally away from the wake.

7.2 Nonlinear system

In the previous section, we confirmed that the resolvent-based kernels, derived from the resolvent operator, provide accurate estimates for the linear system. We now shift our focus to the actual (nonlinear) system, where it is crucial to statistically account for the nonlinear terms using colored forcing. We do so by using the data-driven approach described in §5.2, which is equivalent to the operator-based method with the appropriate forcing CSD \hat{F} . As discussed earlier, we consider both clean and noisy freestream conditions for the nonlinear system, as illustrated in figures 15(a) and (b). The flow is simulated using DNS with the same numerical setup described in §2. Since the estimator is defined in terms of perturbations to the mean, the mean is removed from the sensor readings before convolution with the estimation kernels.

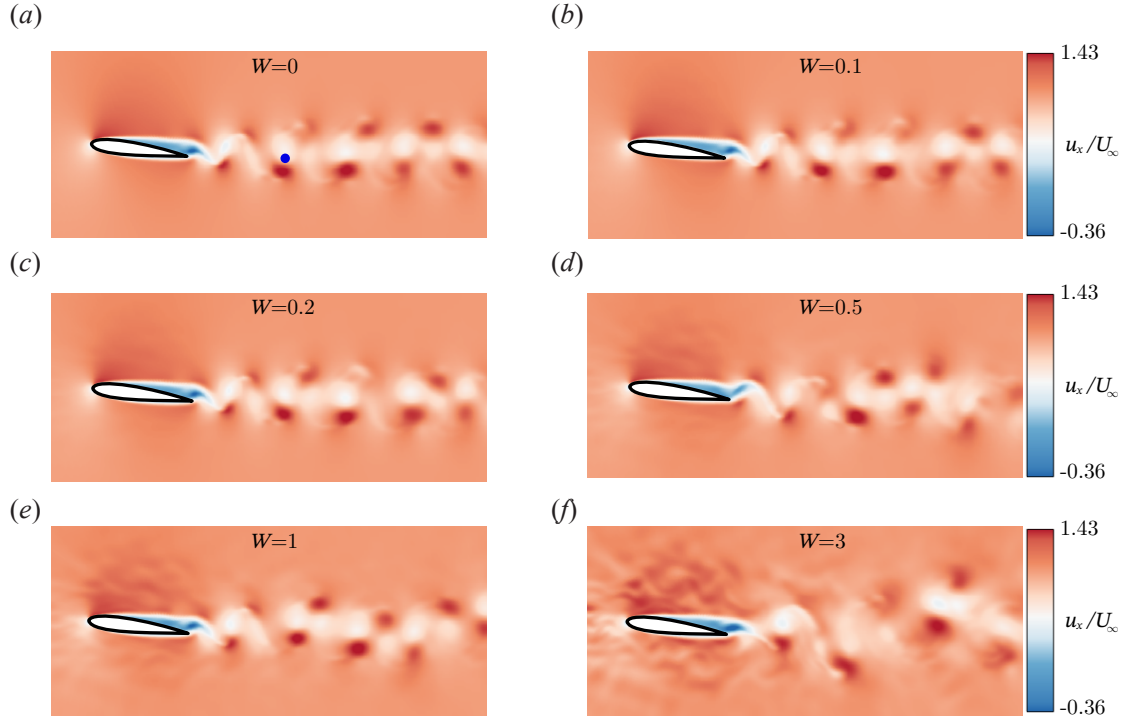


FIGURE 16: Instantaneous snapshots of the streamwise velocity u_x for varying freestream noise intensities, as determined by the forcing amplitude W : (a) $W = 0$ (clean), (b) $W = 0.1$, (c) $W = 0.2$, (d) $W = 0.5$, (e) $W = 1$, and (f) $W = 3$. The blue dot in (a) indicates the location for which the PSD is analyzed in figure 17.

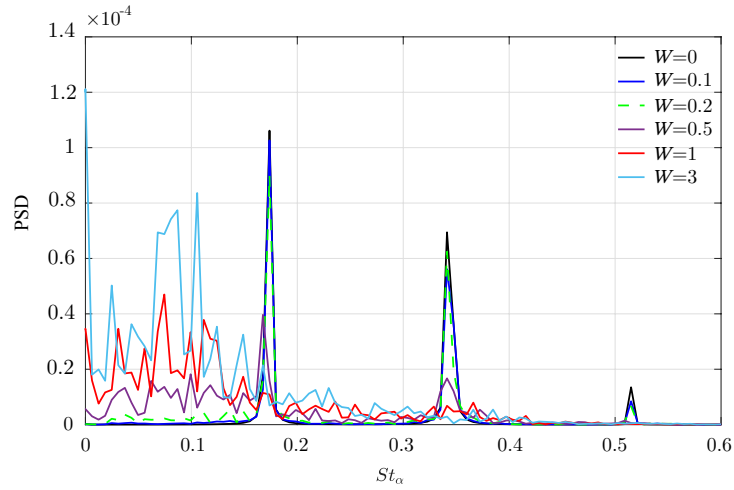


FIGURE 17: Power spectral density of the streamwise velocity u_x for the nonlinear system in terms of the noise level W at the point $[x/L_c, y/L_c] = [2.11, -0.11]$ in figure 16.

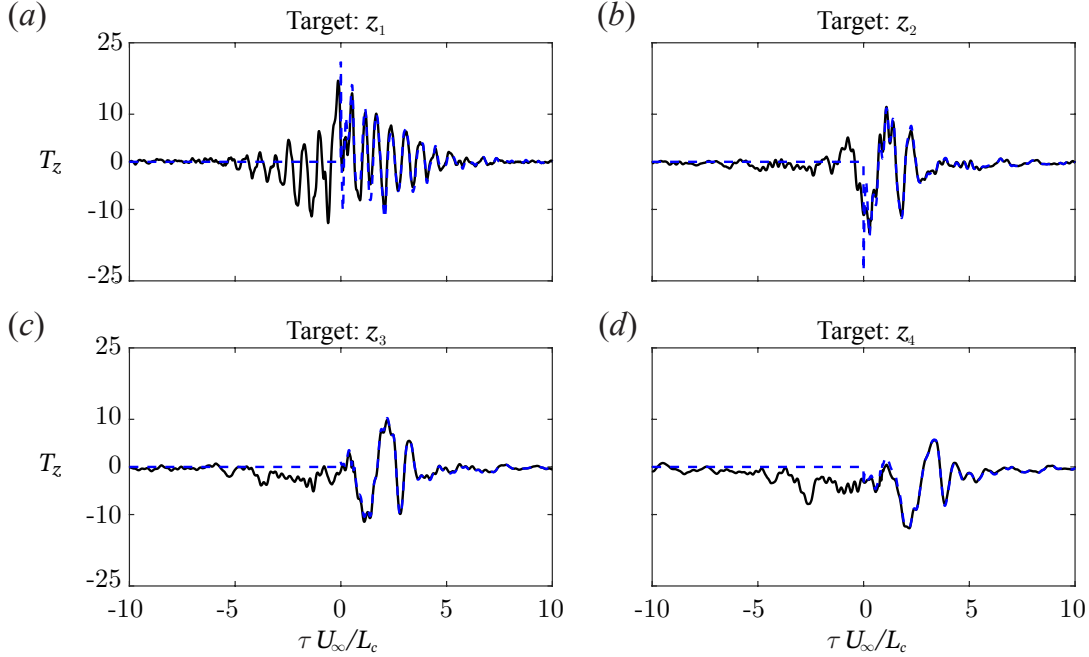


FIGURE 18: Estimation kernels with a colored forcing statistics: non-causal (black solid line) and causal (blue dashed line) kernels between (a) y_1 [$x/L_c = 0.5$] and z_1 [$x/L_c = 1.2$], (b) z_2 [$x/L_c = 2.0$], (c) z_3 [$x/L_c = 3.0$], and (d) z_4 [$x/L_c = 4.0$].

7.2.1 Nonlinear response to the external forcing

The nonlinear system subject to external forcing can be expressed as

$$\frac{\partial \mathbf{q}}{\partial t} = \mathcal{F}(\mathbf{q}) + \mathbf{B}_{f,ext} \mathbf{f}_{ext}. \quad (7.4)$$

We choose the external forcing $\mathbf{f}_{ext}(x, t)$ to be white noise in space and time, generated using random vectors with each entry uniformly distributed over $[-1, 1] \times W$, where W controls the variance of the random vector, adjusting the noise level of the freestream. The CSD matrix for this forcing is $\hat{\mathbf{F}}_{ext} = W^2 \mathbf{I}$. In contrast, the linear system models the nonlinear terms as white noise (an identity matrix) [McKeon and Sharma, 2010].

To help us select an appropriate forcing amplitude W , we analyze the PSD of the state for varying noise levels, focusing on the impact on the vortex shedding. The snapshots in figure 16 demonstrate that while vortex shedding persists at all noise levels, the spatial periodic pattern in the streamwise direction is disrupted. Figure 17 makes this point quantitative by showing the PSD of the state at the location indicated in figure 16(a). The results confirm that the vortex shedding frequencies ($St_\alpha \approx 0.17 \times n$ with $n = 1, 2, 3$) are suppressed for $W \geq 1$, indicating a strong nonlinear modification to the linear dynamics. We select $W = 1$ as the noise level for our estimation and control studies.

7.2.2 Building estimation kernels with colored-forcing statistics

In §7.1.1, we assumed the forcing CSD matrix $\hat{\mathbf{F}}_{nl}$ to be white noise (an identity matrix), resulting in kernels equivalent to a Kalman filter. To enhance the accuracy of the estimation kernels, the resolvent-based framework enables us to incorporate colored forcing statistics via a non-identity $\hat{\mathbf{F}}_{nl}$, which can be obtained in §6.3. Once the nonlinear terms $\hat{\mathbf{f}}_{nl}$, such as those shown in figure 35 in appendix C, are available, we compute $\mathbf{R}_{yf} \hat{\mathbf{F}}_{nl} \hat{\mathbf{R}}_{yf}^\dagger$ and $\mathbf{R}_{zf} \hat{\mathbf{F}}_{nl} \hat{\mathbf{R}}_{zf}^\dagger$ during the two-stage run outlined in 5.1.2.

Alternately, we can implement the data-driven approach [Martini et al., 2022] to obtain estimation kernels that automatically include the influence of the colored-forcing statistics [Zare et al., 2017, Towne et al., 2020, Martini et al., 2022]. The necessary sensor and target data are directly collected from DNS, and Welch’s method [Welch, 1967] is employed to obtain the CSD tensors required to construct the estimation kernels. The time series are divided into 64 blocks of length $tU_\infty/L_c = 5$, with 50% overlap. All other parameters for building the kernels and Wiener-Hopf factorization are consistent with those used in the operator-based approach.

The estimation kernels that account for colored nonlinear forcing are shown in figure 18 for the same sensor and target configuration as was used for the white noise case, i.e., the sensor y_1 [$x/L_c = 0.5$] and the targets z_1, z_2, z_3 , and z_4 [$x/L_c = 1.2, 2.0, 3.0, 4.0$], as shown in figure 15. The figure shows results for the noisy freestream case. As discussed in §7.2.1 and shown in figures 35(d) in appendix C, there is a higher degree of nonlinear interaction near the trailing edge. In this region, the estimation kernel with colored forcing peaks at $\tau U_\infty/L_c < 0$, i.e., the kernel is highly non-causal. This can be alleviated by using the Wiener-Hopf method to optimally enforce causality. Further downstream in the wake in figure 18(b), (c), and (d), the kernels exhibit simpler behavior and distinct peaks, which indicate the travel time of the fluctuations. The difference between the causal and non-causal kernels is small when the target is set further downstream in the wake, where the convective nature of the flow makes the kernels naturally (almost) causal. This trend is similar to the backward-facing step flow reported by Martini et al. [2022].

7.2.3 Single-sensor estimation results for the nonlinear system

We assess the estimation accuracy for the nonlinear system for a single sensor as a function of its location on the surface of the airfoil. Figures 19(b) (clean freestream) and (c) (noisy freestream) show the averaged estimation errors for four sets of targets (A, B, C, and D) shown in figure 19(a). The errors are about an order of magnitude lower for the clear freestream than for the noisy freestream. Imposing external forcing leads to higher-energy fluctuations in the wake, as illustrated in figure 34(c), which increases the impact of nonlinearity and deteriorates the estimation accuracy as the target is moved downstream (estimation error: $D > C > B > A$ in figure 19(b)). In contrast, the error for the clean freestream is non-monotonic with downstream distance: it is lowest for the nearest set of targets, increases, and then decreases again. This latter decrease in error is likely due to the increasingly low-rank behavior of the wake with increasing downstream distance for the clean inflow case.

The recirculation bubble impacts the sensors differently for the clean and noisy freestream cases. For the clean freestream results in figure 19(b), sensors positioned within the recirculation region $0.6 < x/L_c < 1$ [Marquet et al., 2022], show reduced accuracy. However, this effect is not as evident for the noisy freestream case in figure 19(c). This suggests that, whereas the recirculation bubble shields the sensors in the clean freestream case, incoming fluctuations from the noisy freestream instantaneously penetrate the bubble and later contribute to the wake dynamics, providing useful information to the sensors. Among the sensors on the suction surface for the noisy freestream in figure 19(c), those positioned before the separation bubble ($0.2 < x/L_c < 0.5$) and near the trailing edge ($0.8 < x/L_c < 1.0$) most effectively predict the wake dynamics. Notably, rear sensors on the pressure surface also show high estimation accuracy.

7.2.4 Multi-sensor estimation results for the nonlinear system

Next, we present estimation results for the nonlinear system with clean and noisy freestream conditions using multiple sensors. In appendix D, we empirically evaluate six candidate sensor configurations guided by the single-sensor results from the previous section. Ultimately, we selected candidate 6, as defined in Table 3. Since we are interested in vortex shedding, we report estimation results for both components of velocity that would be needed to compute vorticity.

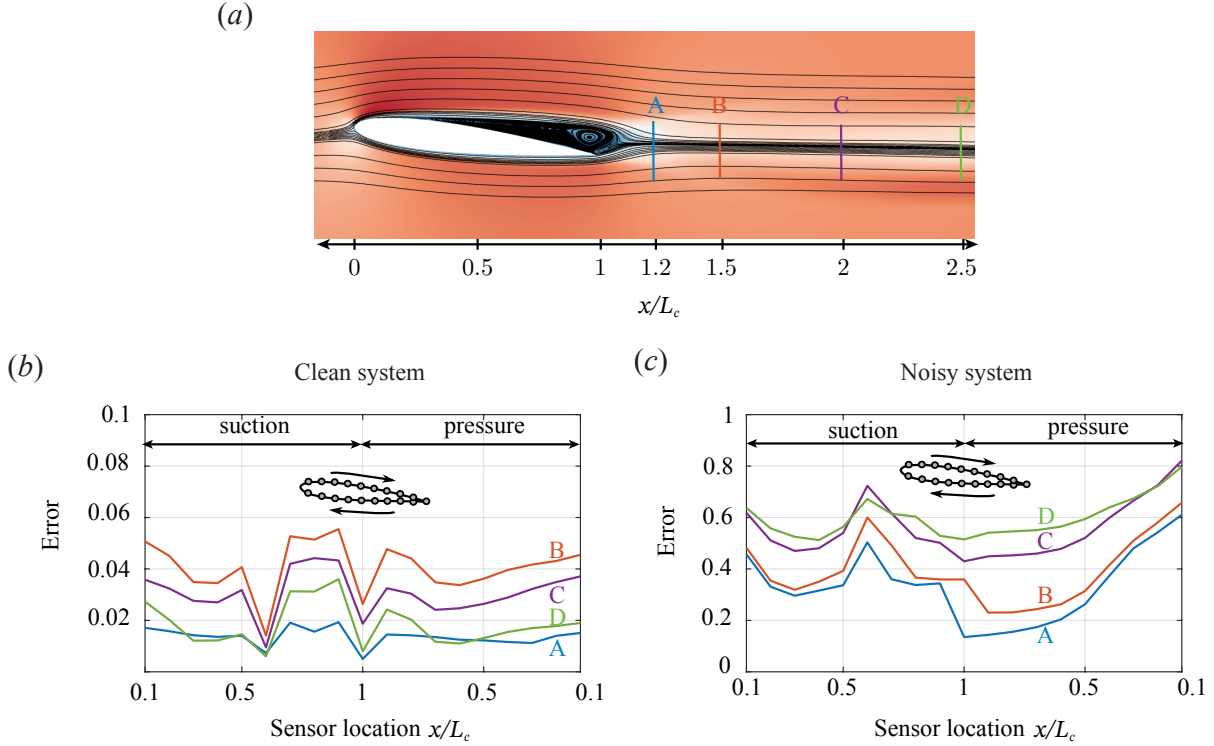


FIGURE 19: Streamline of the flow is shown along with four sets of targets: A ($x/L_c = 1.2$), B ($x/L_c = 1.5$), C ($x/L_c = 2.0$), and D ($x/L_c = 2.5$). Averaged estimation errors are reported for these four lines (A, B, C, and D), which are based on sensor locations on the airfoil surfaces. Panel (b) illustrates the clean system, while panel (c) depicts the noisy system.

Figures 20 and 21 present the causal resolvent estimation of u'_x (left column) and u'_y (right column) comparing with other methods and the true target reading (from DNS) for the clean and noisy freestream inflows at the target points ($x/L_c = 1.2, 2.0, 3.0, 4.0$) aligned with the trailing edge, shown in the top of each figure. The clean DNS system is well estimated using the causal resolvent-based approaches. The Kalman filter captures the dominant frequency's high-energy parts effectively but lacks spatial and temporal detail due to treating the nonlinear terms as white noise. The target near trailing edge, where nonlinearity is strongest in figure 34 in appendix C, is poorly estimated using the Kalman filter, shown in 21(a), while the poor estimates obtained using the TNC approach are due to the presence of substantial amplitude of the noncausal kernels in the non-causal part $\tau U_\infty/L_c < 0$). However, the truncated non-causal kernels include the impact of the colored forcing statistics, making them effective when the kernels are mostly naturally causal for the further downstream target locations, e.g., in the case of 21(e) and (g). Comparing left and right panels in figures 20 and 21, we observe that the cross-stream velocity is estimated more accurately than the streamwise velocity.

Figure 22 provides a more quantitative assessment of the estimation performance by showing the estimation error for each method as a function of the target position for both velocity components in the clean and noisy freestream cases. Notably, the causal resolvent-based approach estimates both velocity components in the clean system with high accuracy. In the noisy system, the estimation accuracy decreases as the distance between the sensor and the target increases downstream. The causal resolvent-based approach enhances estimation accuracy near the trailing edge, where the lack of causality of the optimal noncausal estimator and the effects of nonlinearity are most significant.

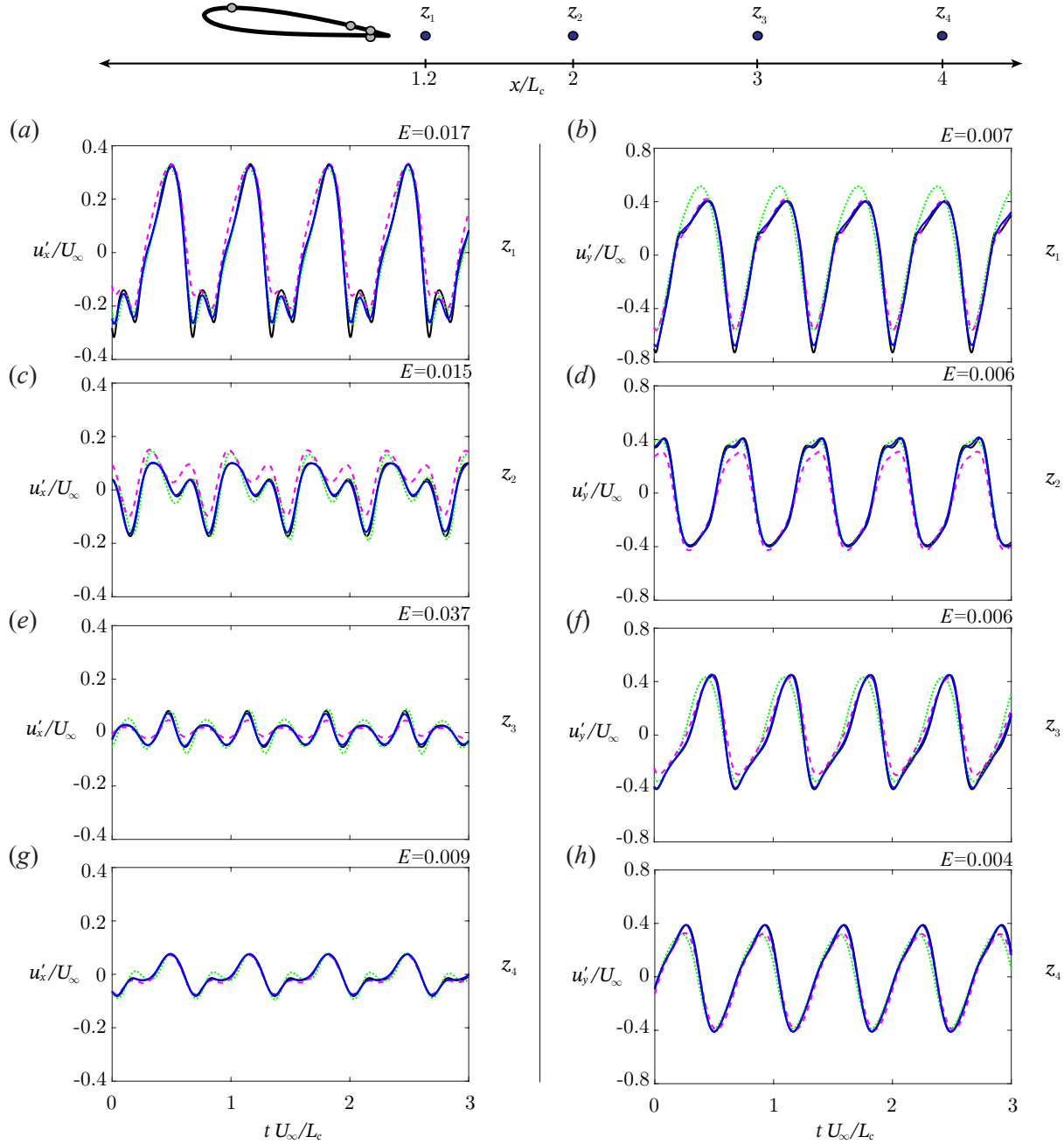


FIGURE 20: Estimation of u'_x (left column) and u'_y (right column) for the nonlinear system with a clean freestream for four targets (columns). Lines: (black solid) true target from the DNS; (green dashed) Kalman filter estimates; (magenta dashed) truncated non-causal estimates; (blue solid) resolvent-based causal estimates. The target locations are: (a), (b) $[z_1 = x/L_c, y/L_c] = [1.2, -0.11]$; (c), (d) $[2.0, -0.11]$; (e), (f) $[3.0, -0.11]$; and (g), (h) $[4.0, -0.11]$, as shown in the top figure and figure 15. The estimation errors for the resolvent-based method are noted in the top-right corner of each panel.

Using the same four shear stress sensors, we estimate the velocity fluctuations u'_x and u'_y for an extended region of the wake in both clean and noisy nonlinear systems. The sensors are positioned near the trailing edge, allowing us to estimate the region behind $x/L_c > 0.8$. We present two snapshots of the estimation,

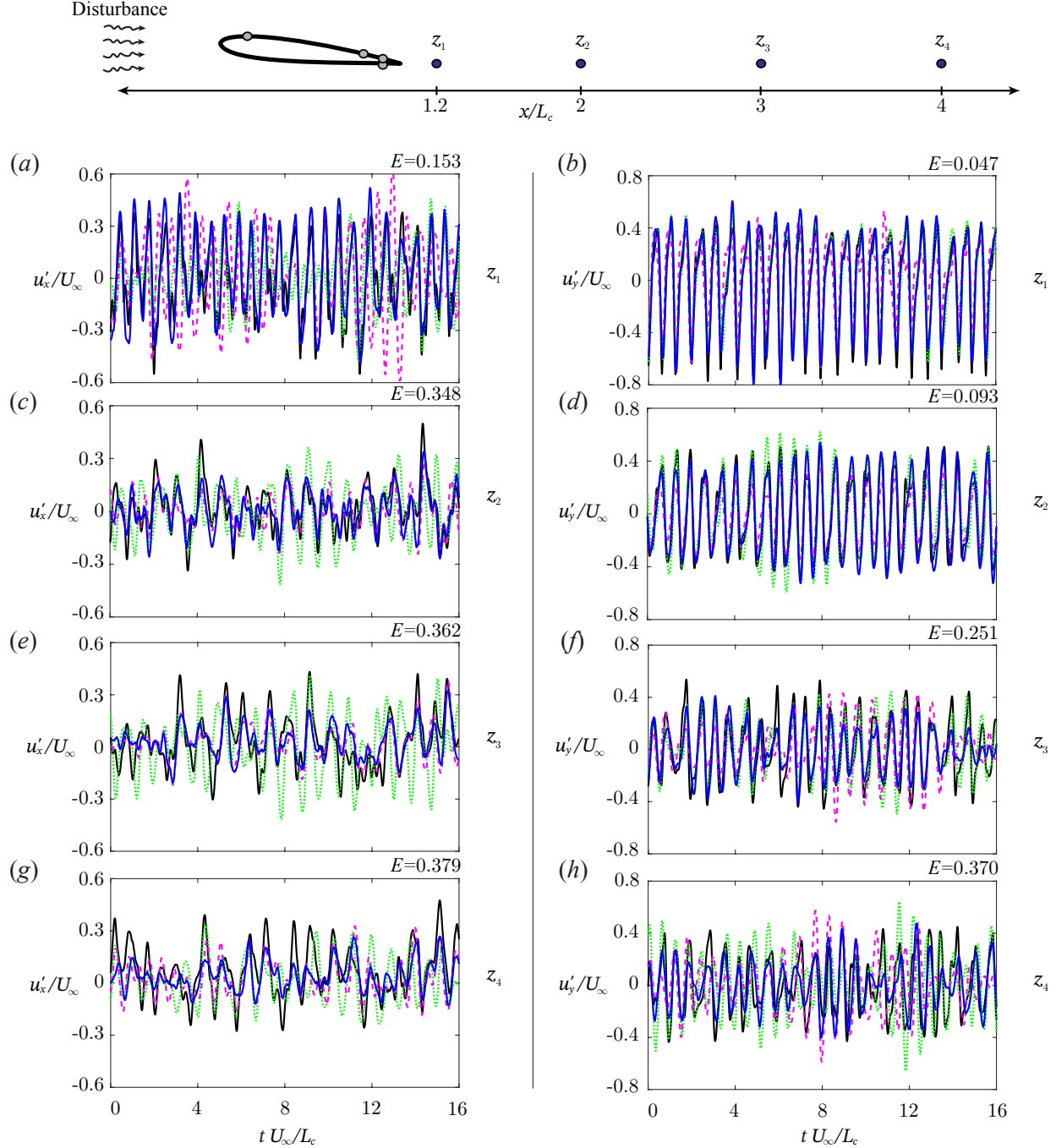


FIGURE 21: Estimation of u'_x (left column) and u'_y (right column) for the nonlinear system with the noisy freestream. The black (solid) line shows the true DNS, while the other lines represent different methods: green (dashed) for Kalman filter, magenta (dashed) for truncated non-causal estimation, and blue (solid) for causal estimation (our method). The target locations are: (a), (b) at $[z_1 = x/L_c, y/L_c] = [1.2, -0.11]$; (c), (d) at $[2.0, -0.11]$; (e), (f) at $[3.0, -0.11]$; and (g), (h) at $[4.0, -0.11]$, as shown in the top figure and figure 15. The estimation errors for the causal method are noted in the top right corner of each panel.

selected to represent different phases of the vortex shedding. For the clean system, our estimation results for u'_x , as shown in figure 23, are highly accurate. In the noisy nonlinear system, however, the estimation

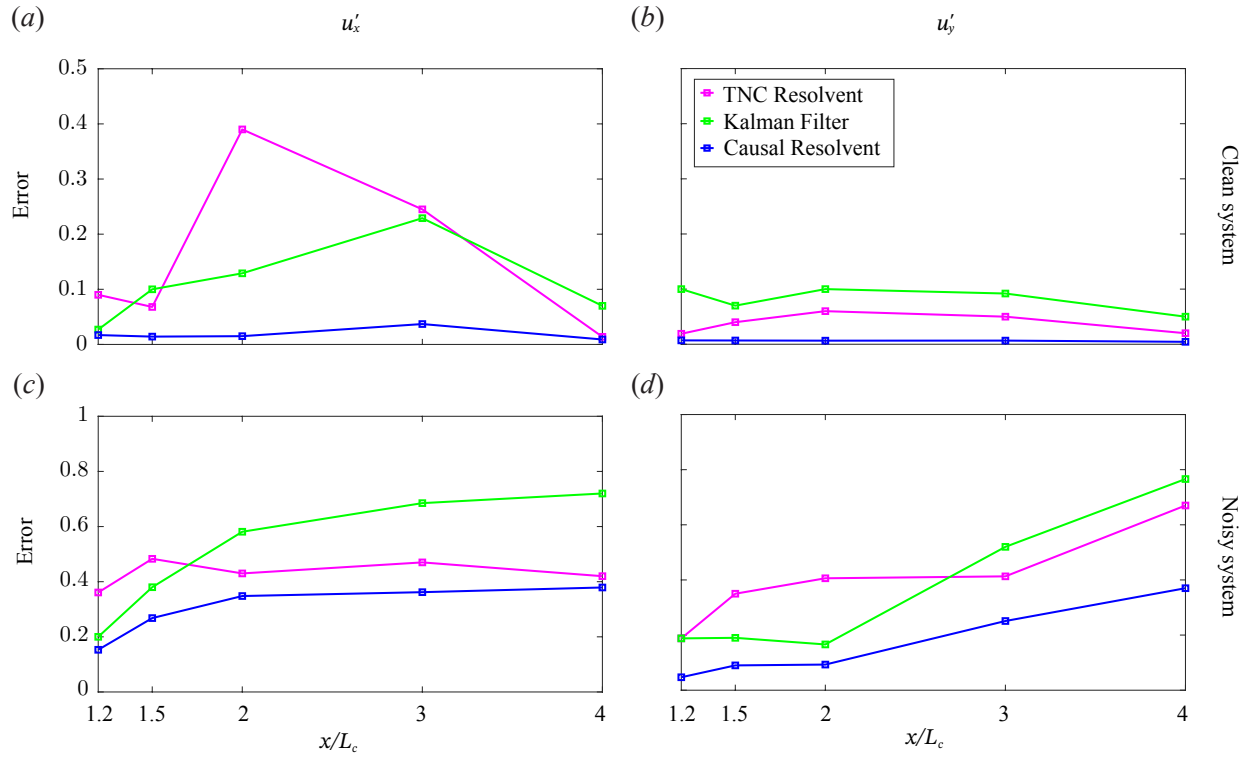


FIGURE 22: Estimation errors for nonlinear systems: (a) u'_x and (b) u'_y for clean freestream; (c) u'_x and (d) u'_y for noisy freestream. Blue lines represent causal resolvent-based estimation, while magenta and green lines denote truncated non-causal estimation using colored forcing and a Kalman filter (white noise), respectively.

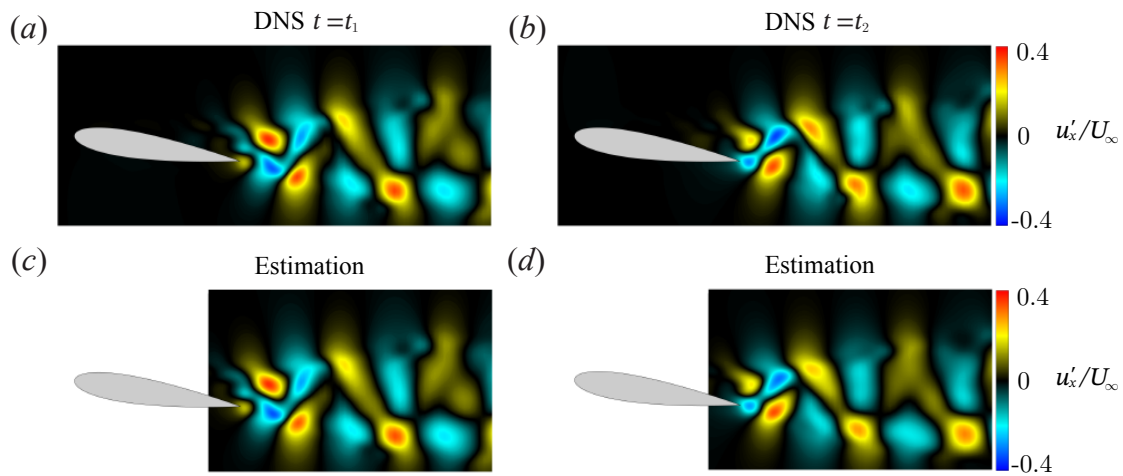


FIGURE 23: Estimation of the streamwise velocity fluctuation u'_x in an extended wake region for the nonlinear system with a clean freestream at two times: top row shows DNS results, and the bottom row shows results from causal resolvent-based estimation.

accuracy decreases due to perturbations that disrupt the vortex structure. Despite the challenges posed by chaotic fluctuations within the wake, the causal resolvent-based approach effectively estimates the wake flow, as demonstrated in figures 24.

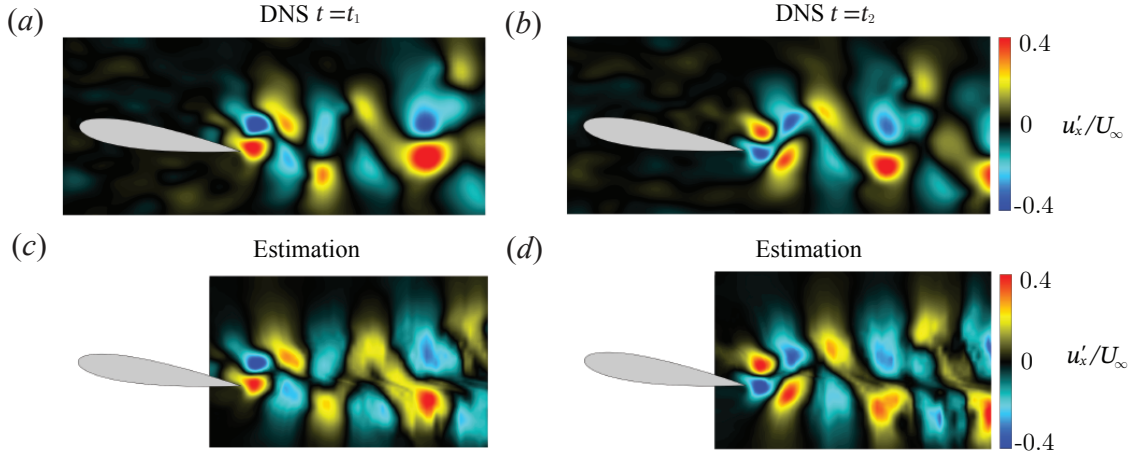


FIGURE 24: Estimation of the streamwise velocity fluctuation u'_x in an extended wake region for the nonlinear system with a noisy freestream at two times: top row shows DNS results, and the bottom row shows results from causal resolvent-based estimation.

8 Resolvent-based control results

In this section, we use the resolvent-based controller described in §4.3 to suppress velocity fluctuations in the wake. Active flow control methods using blowing/suction, synthetic jets, and plasma actuators have been successfully used to suppress laminar vortex shedding behind bluff bodies in both experimental [Ffowcs Williams and Zhao, 1989, Tao et al., 1996, Strykowski and Sreenivasan, 1990, Min and Choi, 1999, Fujisawa et al., 2001] and numerical studies [Roussopoulos and Monkewitz, 1996, Lin and Tsai, 2024]. Suppressing vortex shedding significantly reduces lift and drag fluctuations, attracting considerable engineering interest. We seek to mitigate velocity fluctuations in the wake, which naturally includes the influence of vortex shedding.

Resolvent analysis has been fruitfully used to guide open-loop control efforts by suggesting effective forcing frequencies and actuator locations to which the flow is responsive [Yeh and Taira, 2019, Gross et al., 2024] for open-loop control. Instead, we wish to design closed-loop controllers that react in real time to broadband frequency content within the flow. Using the estimated flow state from the resolvent-based estimator, implicitly included in the resolvent-based controller, the controller determines the actuation that most effectively cancels the target values, an approach also known as reactive control or the wave-canceling method [Sasaki et al., 2018a,b, Morra et al., 2020, Martini et al., 2022, Audiffred et al., 2023]. As before, we first control the linear system before considering the actual nonlinear problem under noisy freestream conditions. We show that the optimal causal resolvent-based controller significantly outperforms a truncated non-causal controller, especially when using a pair of nested controllers to account for mean-flow modifications.

8.1 Control set-up

Our overall control architecture is shown schematically in figure 25. Some closed-loop controllers used to suppress wake fluctuations rely on impractically located sensors, e.g., behind the body in the wake itself. Our resolvent-based controller avoids this issue by implicitly using the resolvent-based estimator to predict the evolution of disturbances using shear-stress sensors on the airfoil surface. Our actuators mimic unsteady blowing and suction at discrete positions on the surface of the airfoil, modeled as compact source terms (again with Gaussian spatial support) in the momentum equations. As shown earlier in figure 16, the control

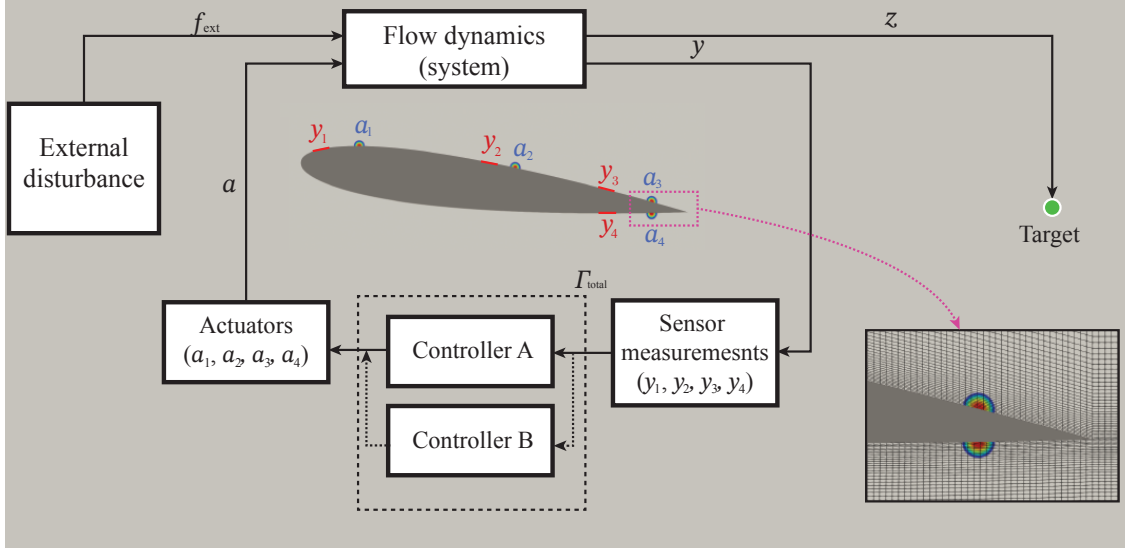


FIGURE 25: Control scheme for resolvent-based control of the flow around a NACA0012 airfoil. Red markers indicate shear-stress sensors, while contoured circles represent actuators in the form of momentum sources with Gaussian spatial support on the airfoil surface. The green circle marks the target location. For the control of the nonlinear system, we use a second nested controller (controller B) designed for the modified mean flow produced by the original controller (A). The insert highlights the grid resolution around the rear actuators.

signal is computed and applied online during the simulation.

In choosing the placement of our sensors and actuators, we account for the combined amplifier and oscillator characteristics of this flow [Schmid and Sipp, 2016]; the linear operator is globally stable, such that upstream disturbances are convectively amplified as they travel downstream, but it also contains a single lightly damped mode that generates amplifier-like vortex shedding. The sensor and actuator near the leading edge are designed to disrupt the recirculation bubble and suppress the global vortex-shedding behavior [Broglia et al., 2018, Déda et al., 2023]. The sensors and actuators near the trailing edge are designed to mitigate freestream fluctuations before they are amplified in the wake. We position the front sensors and actuators near the leading edge similarly to prior works [Colonius and Williams, 2011, Broglia et al., 2018, Yeh and Taira, 2019, Asztalos et al., 2021], while the positions of the rear sets are motivated by our estimation work.

For the nonlinear problem, the actuation modifies the mean flow via triadic interactions, even if the actuation itself is zero-mean. This presents a challenge since the controller is derived based on linearization about the original (uncontrolled) mean flow and is designed to minimize fluctuations to that mean. However, our primary objective remains to minimize the flow unsteadiness at the targets, i.e., the velocity fluctuations about the modified (controlled) mean flow. To address this challenge, we use an iterative approach similar to that of Leclercq et al. [2019]. After applying the controller based on the original (uncontrolled) mean flow (labeled as controller A in figure 25), we design a second controller based on the new mean flow (controller B) and wrap it around the system that is still under the influence of controller A. The combined influence of the two controllers can be thought of as a single new nested controller that takes in the sensor measurements and drives the actuators. This iterative process can be repeated any number of times, but we achieve satisfactory results with just two nested controllers.

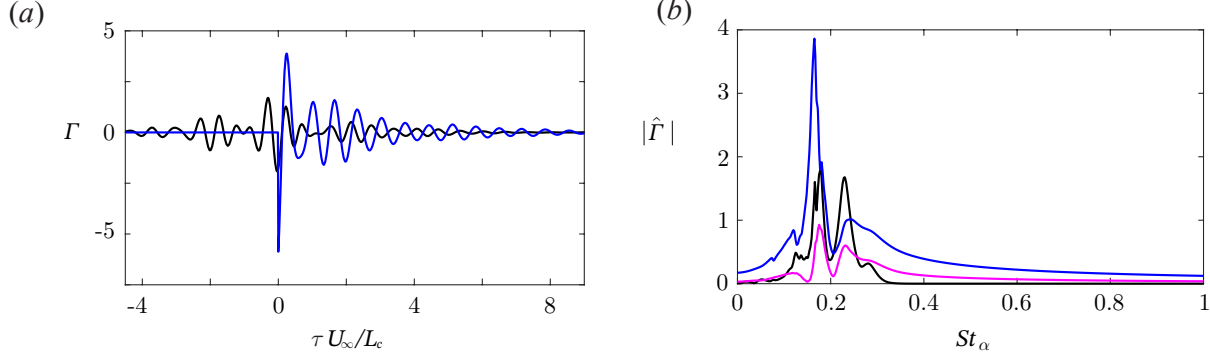


FIGURE 26: Control kernels with the sensor positioned near the trailing edge (y_3) and the target z located at $x/L_c = 1.5$ in the time (a) and frequency (b) domains. The black line represents the non-causal control kernel, the magenta line shows the truncated non-causal kernel, and the blue line depicts the causal control kernel computed using the Wiener-Hopf method.

Following our previous work [Martini et al., 2022], we quantify the controller performance via the metric

$$\varepsilon_{\text{con}} = 1 - \frac{\sum_i \int (z_{i,\text{con}}(t))^2 dt}{\sum_i \int (z_{i,\text{uncon}}(t))^2 dt}, \quad (8.1)$$

which measures the reduction in fluctuation energy at the targets compared to the uncontrolled flow.

8.2 Control of the linear system

We first consider the linear system obtained by linearizing the Navier-Stokes equations about the uncontrolled mean flow subject to external forcing, as in §7.1. For the linear system, we use only controller A and just two actuators (a_3 and a_4). The resolvent-based control kernels are obtained using the operator-based approach described in 5.1. The direct and adjoint runs are conducted over the interval $tU_\infty/L_c \in [-48, 48]$.

Figure 26 shows the non-causal and causal control kernels kernel between the y_3 sensor and a_3 actuator for a target z at $x/L_c = 1.5$ in the time and frequency domains. In figure 26(a), due to the close proximity of the sensor and actuator, the non-causal control kernel contains relatively large values in the non-causal part $\tau U_\infty/L_c < 0$. This issue is moderated using the Wiener-Hopf method, similar to the estimation kernels. For the causal kernel, the current measurement significantly impacts the actuation signal [Morra et al., 2020, Martini et al., 2022]. Figure 26(b) presents the control kernels in the frequency domain. The truncated non-causal control kernel (magenta line) shows a considerable loss in magnitude, while the causal control kernel significantly amplifies the sensor measurement at the vortex shedding frequency $St_\alpha = 0.17$. As expected, increasing the actuation cost \mathbf{P} reduces the relative magnitude of the control kernel, leading to a smaller actuation force. We set $\mathbf{P} = \epsilon I$ with $\epsilon = 10^{-1}$ of the maximum value of \mathbf{R}_{z_a} .

Figure 27 presents the time-series data for the controlled and uncontrolled streamwise and cross-streamwise velocity fluctuations at the target. While the truncated non-causal controller achieves modest improvements, the causal resolvent-based control significantly reduces both velocity components. The power spectral density (PSD) of the uncontrolled and controlled streamwise velocity is shown in figure 28(a). The causal resolvent-based controller effectively suppresses the dominant vortex shedding frequency, while the truncated non-causal controller fails to accomplish this. Using the causal approach, the two actuators at the trailing edge reduce the turbulent kinetic energy of the velocity fluctuations at the target, as measured by (8.1), by 85%. In contrast, the truncated non-causal approach achieves only a 27% reduction. In terms of

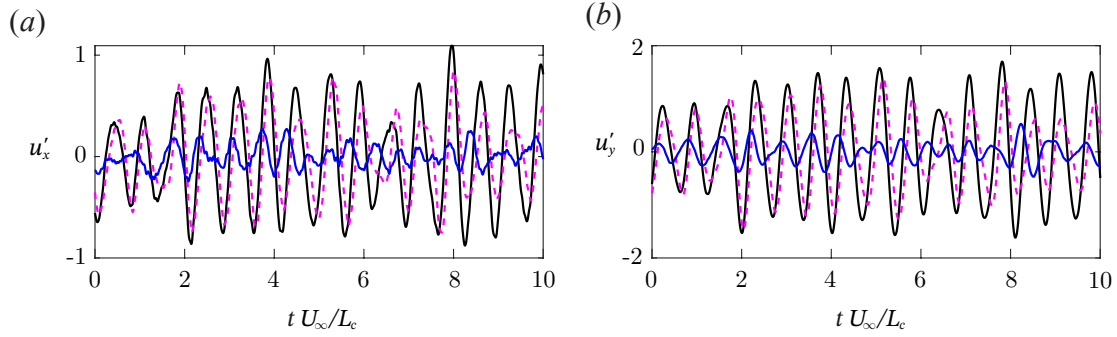


FIGURE 27: Time-series of velocity fluctuations for the uncontrolled and controlled linear systems: (a) u'_x ; (b) u'_y . Lines: uncontrolled (black line), truncated non-causal control (magenta dashed line), and causal control (blue line).

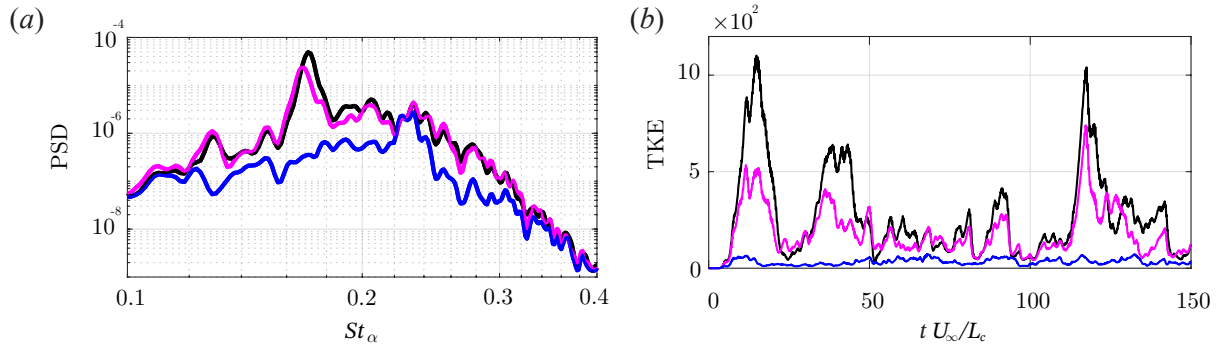


FIGURE 28: Control performance for the linear system: (a) PSD of the streamwise velocity fluctuations u'_x for the controlled (blue) and uncontrolled (black) cases, with the magenta line representing the truncated non-causal control approach; (b) Turbulent kinetic energy (TKE) integrated over the wake region.

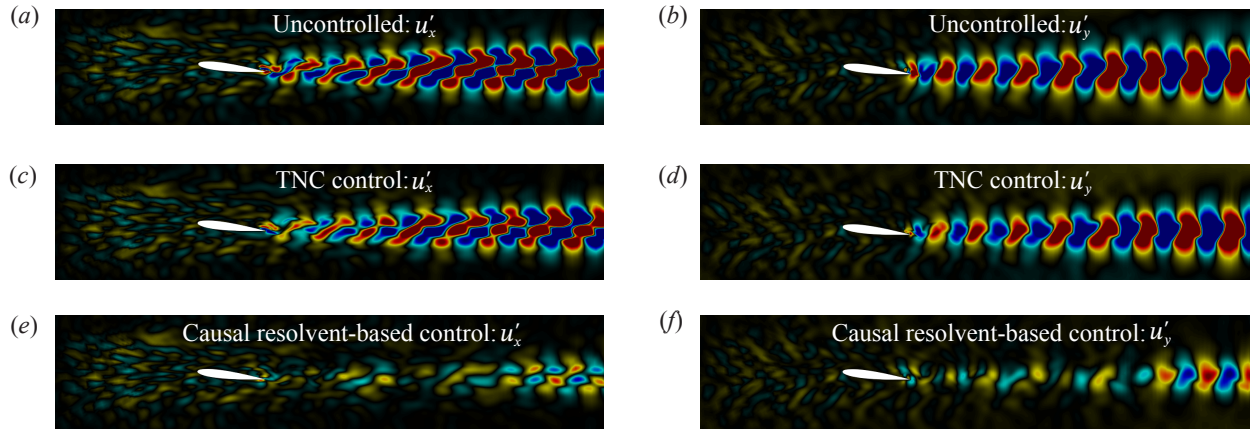


FIGURE 29: Snapshots of the streamwise and cross-streamwise velocity fluctuation fields for the linear system: (a,b) uncontrolled; (c,d) truncated noncausal (TNC) control; (e,f) causal resolvent-based control.

RMS velocities, the causal controller achieves a 62% decrease, compared to around 14% for the truncated non-causal controller.

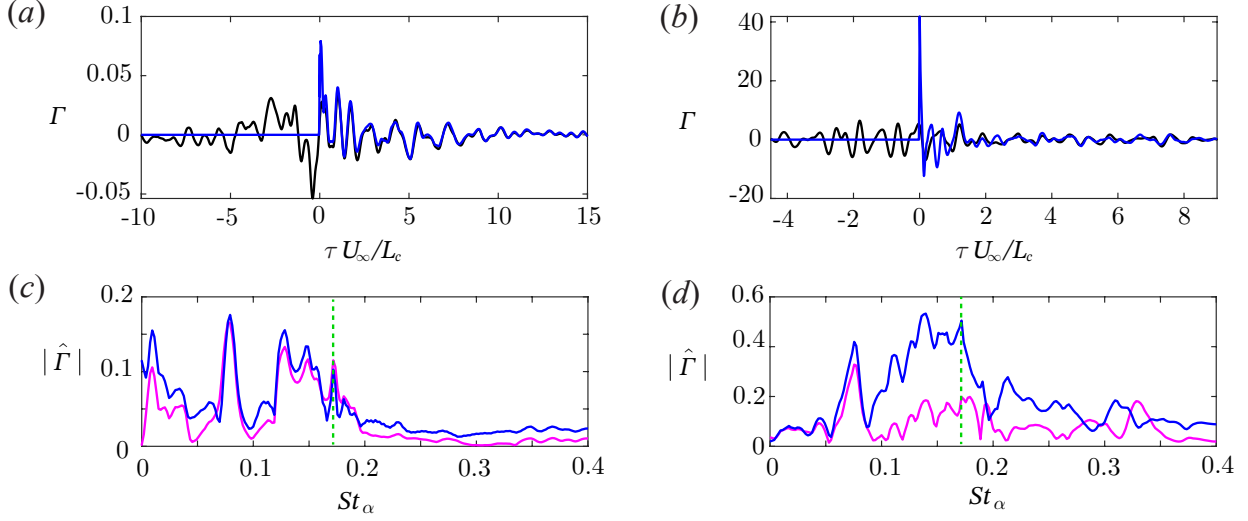


FIGURE 30: Control kernels for the nonlinear system: (a) and (b) display the kernels in the time domain, while (c) and (d) present them in the frequency domain. Specifically, (a) and (c) correspond to y_3 and a_3 , and (b) and (d) correspond to y_4 and a_4 , as shown in figure 25. The green dashed line in c and d indicates the vortex shedding frequency.

While the controller is designed to minimize the velocity fluctuations at the target, it also does so over an extended region of the wake. Figure 29 presents instantaneous snapshots of u'_x and u'_y for the controlled and uncontrolled systems. The wake modes excited by the upstream-generated external disturbance are effectively suppressed by the actuation at the trailing edge, as illustrated in figure 29(e) and (f). To make this reduction quantitative, the turbulent kinetic energy (TKE) integrated over the wake region ($x/L_c = [1.1, 5]$, $y/L_c = [-1, 1]$) is shown as a function of time in figure 28(b).

8.3 Control of the nonlinear system

The ultimate goal of this work is to reduce the wake fluctuations in the nonlinear system (DNS) using the optimal linear resolvent-based controller. As discussed earlier, we use a second controller (controller B) to account for the impact of the first controller on the mean flow. After turning on the first controller, we wait until the flow achieves a new statistical steady state before turning on the second controller. The actuator outputs are determined by resolvent-based control kernels, with an additional constant forcing applied to the two front actuators to destroy the separation bubble. The data-driven approach is used to build the resolvent-based kernels to account for the colored nonlinear forcing. The operator approach is used to compute \mathbf{R}_{ya} and \mathbf{R}_{za} , required in (5.19). Alternatively, these terms can be obtained using the data-driven approach by running a series of impulse response simulations, as discussed in §5.2. We show results only for the noisy freestream, as our controller entirely stabilizes the flow for the clean freestream case, resulting in a steady flow maintained by a steady actuation signal.

Figure 30 shows the control kernels for two sensor-actuator pairs in the time and frequency domains. The sensor, actuator, and target combination of figure 30(a) and (c) are equivalent to those considered for the linear system in figure 26. Since our sensor and actuator locations are positions close to each other, the peaks of the non-causal kernels are near $\tau U_\infty / L_c = 0$. A notable difference between the kernels for the linear and nonlinear systems (which are different because of the colored nonlinear forcing) is that the vortex-shedding frequency is considerably less prevalent in the nonlinear case, presumably due to the disruption of the vortex shedding by the noisy freestream. Accordingly, the control kernels will amplify a wide range of frequencies

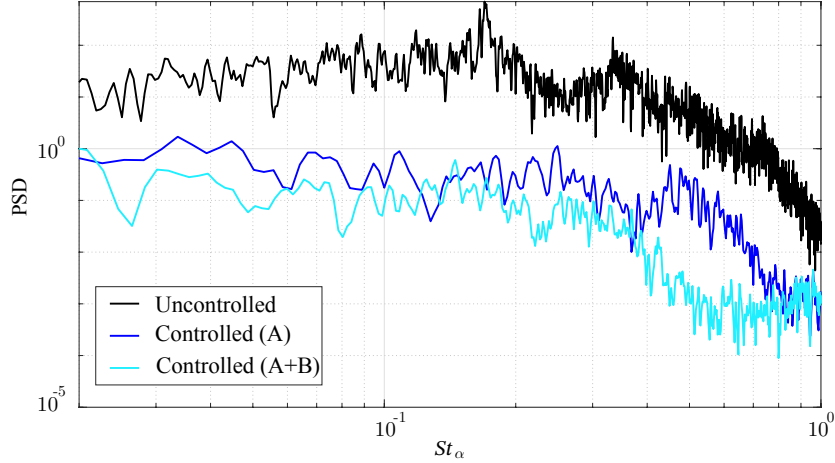


FIGURE 31: PSD of the streamwise velocity fluctuation u'_x at the target z located at $[x/L_c, y/L_c] = [1.5, -0.11]$. The black solid line represents the uncontrolled flow; the blue line shows the controlled flow using Controller A; the cyan line depicts the controlled flow using both controllers (Controller A + Controller B).

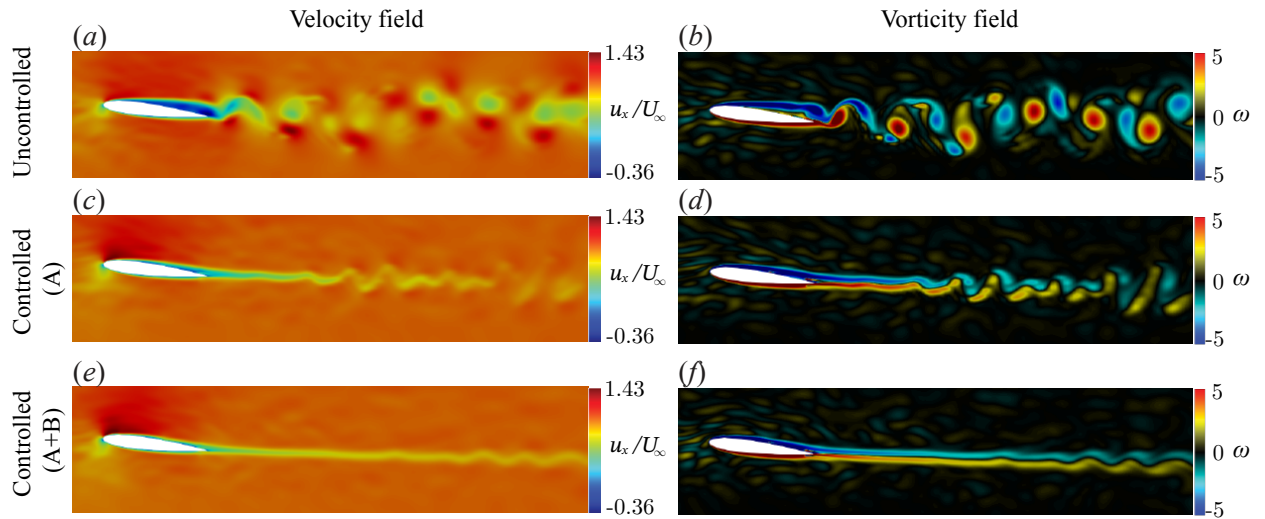


FIGURE 32: Velocity (u_x) and vorticity (ω) fields for the system with noisy freestream inflow. (a) and (b) illustrate the uncontrolled flows; (c) and (d) show the controlled flows using Controller A; (e) and (f) present the controlled flows using both controllers (Controller A + Controller B).

in the sensor readings, producing broadband actuation signals.

Figure 31 shows the PSD of the streamwise velocity at the target for the uncontrolled and controlled flows. Both the single and nested controllers significantly reduce the energy of velocity fluctuations for $St_\alpha < 1$. The control performance, measured by the metric in (8.1) representing the reduction in velocity fluctuation energy, reaches approximately 94% with Controller A. By incorporating a second controller (Controller A + B), the performance improves further, achieving 98% reduction in fluctuation energy at the target. The reduction in RMS velocity is 78% using Controller A and 90% using both Controllers A and B. As shown in figure 31, this improvement further mitigates target fluctuations at higher frequencies ($0.4 < St_\alpha < 0.7$),

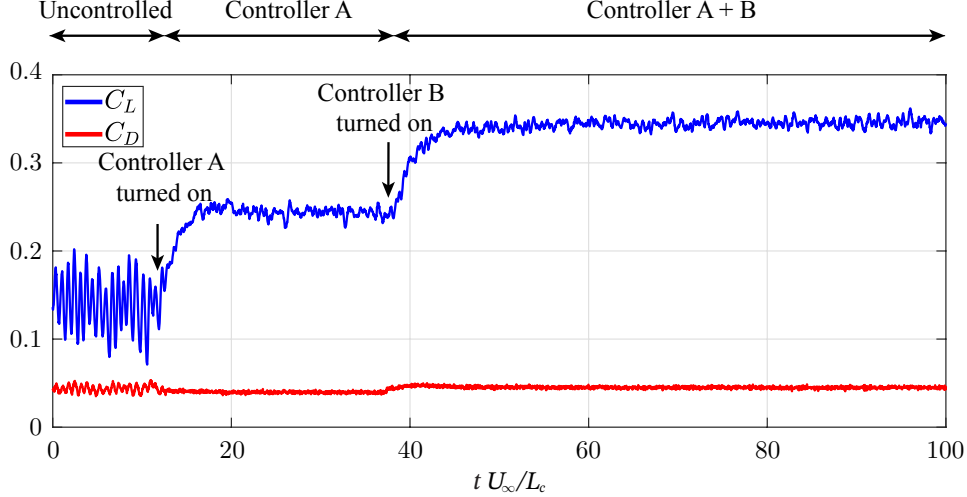


FIGURE 33: Lift and drag coefficients for the uncontrolled and controlled flow over time.

which originate further downstream, as we can verify in figure 32.

Figure 32 presents both uncontrolled and controlled snapshots of the streamwise velocity and vorticity. As shown in figure 32(a) and (b), chaotic vortex shedding is prominent in the wake of the uncontrolled flow. However, this can be significantly mitigated by controller A. Introducing controller B further suppresses the oscillating flow downstream ($x/L_c > 2$). In the controlled flow, the mean flow changed, which is essential as the wake fluctuations from vortex shedding originate from the separated flow.

Finally, figure 33 demonstrates the impact of the controllers on the aerodynamic coefficients. The time-averaged lift coefficient (\bar{C}_L) is improved by 143% with the use of Controllers A and B, while the time-averaged drag coefficient (\bar{C}_D) remains largely unchanged. The fluctuations in both coefficients are effectively suppressed by the controllers. Although improving the aerodynamic coefficients was not the primary objective, mitigating wake fluctuations improved the lift coefficient as a welcome byproduct.

9 Conclusions

This work demonstrates the successful application of resolvent-based estimation and control to a two-dimensional NACA 0012 airfoil at $Ma_\infty = 0.3$, $Re_{L_c} = 5000$, and $\alpha = 6.5^\circ$. Under similar assumptions, our estimator and controller converge to the Kalman filter and LQG controller. However, our approach can incorporate the nonlinear terms of the Navier-Stokes equations using colored-in-time statistics, leading to significantly higher estimator accuracy and improved controller performance.

To construct the estimator and controller, we employed two computational approaches: an operator-based approach and a data-driven approach. The operator-based approach is computationally efficient, does not require a priori model reduction, and accounts for the colored statistics of nonlinear terms from the Navier-Stokes equations that act as a forcing on the linear dynamics. The data-driven approach, which circumvents the need to construct linearized Navier-Stokes operators, naturally incorporates these colored statistics of the nonlinear terms. We utilized the Wiener-Hopf formalism to enforce causality, enabling the evaluation of only available measurements, which is an optimal strategy for real-time estimation and control.

This work makes significant contributions to the implementation of resolvent-based frameworks. Specifically, it demonstrates the integration and execution of resolvent-based estimation and control approaches within a compressible flow solver designed for high-performance computing for large-scale problems. First,

the linearized Navier-Stokes operator developed in this work is accurate and applicable for parallel computing, making it a powerful tool for large-scale applications. Second, using a parallel time-stepping approach significantly accelerates computations when handling large-scale linearized Navier-Stokes operators, including using a parallel adjoint solver efficiently. Additionally, the streaming Fourier transform within a solver is valuable for saving memory for constructing cross-spectral densities, which are necessary for building kernels. Another key feature of the tool is its ability to extract the nonlinear terms of the Navier-Stokes equations, offering valuable insights for other methodologies. Lastly, we solve the Wiener-Hopf problems directly within the solver to minimize reliance on post-processing tools such as MATLAB and to enhance computational efficiency by enabling faster routines with reduced memory usage.

Before applying estimation and control to the laminar airfoil, we obtained the mean flow through direct numerical simulation and performed global stability and resolvent analysis around this mean flow. Random upstream perturbations were introduced to disrupt the periodic limit cycle caused by vortex shedding, inducing chaotic fluctuations. We then conducted resolvent-based estimation and control on both linear and nonlinear systems under these conditions.

Our results demonstrate that resolvent-based kernels are effective in estimating and controlling chaotic fluctuations in the wake of an airfoil. The performance of both estimation and control is enhanced when sensors and actuators are strategically placed in effective locations. To determine these effective placements, we investigated estimation errors and employed a streamline strategy. While we addressed the estimation across the entire wake region, we found that controlling the entire region yields results similar to targeting a single point. In the linear system, the estimation error is approximately 8% with two sensors, and the control performance reaches 85% using two actuators. For the nonlinear system, the estimation error increases to 30% with four sensors, while the control performance improves to 98% using four actuators and two controllers. These accomplishments are significant, as they demonstrate the feasibility of applying a new closed-loop control method in a numerical setup and achieving reliable estimation. This work provides a solid foundation for extending the resolvent-based framework to other turbulent flow scenarios.

Future work will focus on optimizing sensor and actuator placements, as well as applying control strategies to turbulent wakes behind an airfoil. In this study, we evaluated effective sensor placement based on estimation error, leading to satisfactory estimation and control results. However, the placement and the number of sensors and actuators have not yet been optimized. Addressing this will require formulating and solving a mathematical optimization problem, which will be considered in future research. Additionally, applying estimation and closed-loop control strategies to turbulent wakes is another area for future exploration. The positive effects of reducing turbulent wakes in terms of aerodynamic performance should be further investigated.

Appendix A Resolution study of the baseflow in terms of eigenvalues

Here, we study the grid convergence of the frequency of the vortex-shedding frequency in the DNS and the eigenvalue of the linear operator \mathbf{A} . N_s is the number of grid points along the suction surface, and N_w is the number of grid points along the streamwise axis in the wake. Due to the need for a fine grid at the downstream target locations, we use a finer grid in the wake region compared to the typical grids with fewer points used in previous studies [Kojima et al., 2020, Marquet et al., 2022]. The Strouhal number (based on the angle of attack) $St_{\alpha, DNS}$ is the vortex-shedding frequency observed in the DNS, and $St_{\alpha, \mathbf{A}}$ is the frequency of the least-stable eigenvalue of the operator \mathbf{A} linearized about the corresponding DNS mean flow. Based on our convergence study, we selected Mesh 5 for this work.

Mesh	N_s	N_w	Total cells	$St_{\alpha, \text{DNS}}$	$St_{\alpha, \mathbf{A}}$
1	100	90	29,704	0.169650	0.168319
2	100	180	43,924	0.168541	0.167249
3	150	135	67,354	0.169124	0.168933
4	200	180	120,204	0.169525	0.169140
5	200	268	148,188	0.169288	0.169241
6	200	300	158,364	0.169211	0.169222
7	200	360	177,444	0.169246	0.169207

TABLE 2: Grid convergence of the DNS vortex shedding frequency and the least-stable eigenvalue of the linear operator \mathbf{A} .

Appendix B Wiener-Hopf Method

B.1 Theoretical Wiener-Hopf decomposition

The Wiener-Hopf method [Noble, 1958] is a mathematical technique extensively used in applied mathematics. It enables the decomposition of arbitrary functions into components corresponding to the upper and lower halves of the complex plane. This paper leverages the Wiener-Hopf method to impose causality on estimation and control kernels, following methodologies outlined by Daniele and Lombardi [2007], Martinelli [2009], Martini et al. [2022].

First, we define the Fourier transform as

$$\hat{f}(\omega) = \int_{-\infty}^{+\infty} f(t)e^{-i\omega t} dt, \quad (\text{B.1})$$

where $\hat{f}(\omega)$ represents an arbitrary function in the frequency domain. This function can be decomposed into $\hat{f}_+(\omega)$ and $\hat{f}_-(\omega)$, which are analytic functions in the lower and upper complex half-planes, respectively. These can also be analyzed in the time domain as:

$$\hat{f}_+(\omega) = \int_0^{+\infty} f(t)e^{-i\omega t} dt, \quad (\text{B.2})$$

$$\hat{f}_-(\omega) = \int_{-\infty}^0 f(t)e^{-i\omega t} dt, \quad (\text{B.3})$$

where the (+) subscript indicates that the function contains values only in the positive time domain, while the (−) subscript denotes that the function contains values only in the negative time domain. Thus, the subscripts (+) and (−) impose causality and non-causality on the function, respectively.

Now, we consider the two Wiener-Hopf problems [Martini et al., 2022] related to this paper’s work,

$$\hat{H}(\omega)\hat{F}_+(\omega) = \hat{\Lambda}_-(\omega) + \hat{G}(\omega), \quad (\text{B.4})$$

$$\hat{K}(\omega)\hat{F}_+(\omega)\hat{H}(\omega) = \hat{F}_-(\omega) + \hat{L}(\omega)\hat{G}(\omega), \quad (\text{B.5})$$

where $\omega = i2\pi f$ with frequency f , and \hat{H} , \hat{G} , \hat{K} , \hat{L} are known matrices (or functions), while $\hat{F}_+(\omega)$ and $\hat{\Lambda}_-(\omega)$ are the unknown matrices (or functions). The objective of the Wiener-Hopf problem is to determine $\hat{F}_+(\omega)$ and $\hat{\Lambda}_-(\omega)$.

To solve the two Wiener-Hopf problems, we employ two types of factorizations. The additive factorization decomposes the matrix into two \pm components, separated only through the addition process

$$\hat{F}(\omega) = (\hat{F}(\omega))_- + (\hat{F}(\omega))_+, \quad (\text{B.6})$$

using the parenthesis $(\cdot)_{\pm}$. The multiplicative factorization, which is not commutative, is performed as

$$\hat{\mathbf{F}}(\omega) = \hat{\mathbf{F}}(\omega)_{-} \hat{\mathbf{F}}(\omega)_{+}, \quad (\text{B.7})$$

where the subscripts (\pm) are used without parentheses. The solutions of the first Wiener-Hopf problems in (B.4) is given by

$$\hat{\mathbf{F}}_{+}(\omega) = \left(\hat{\mathbf{G}}(\omega) \hat{\mathbf{H}}_{-}^{-1}(\omega) \right)_{+} \hat{\mathbf{H}}_{+}^{-1}(\omega), \quad (\text{B.8})$$

where $\hat{\mathbf{H}}_{-}$ is obtained from the reverse multiplicative factorization. For (B.5), the solutions is

$$\hat{\mathbf{F}}_{+}(\omega) = \hat{\mathbf{K}}_{+}^{-1}(\omega) \left(\hat{\mathbf{K}}_{-}^{-1}(\omega) \mathbf{L}(\omega) \mathbf{G}(\omega) \mathbf{G}_{-}^{-1}(\omega) \right)_{+} \hat{\mathbf{H}}_{+}^{-1}(\omega). \quad (\text{B.9})$$

B.2 Numerical Wiener-Hopf decomposition

To ensure a seemly, fully parallelized workflow, we solve the Wiener-Hopf problems [Noble, 1958] used to enforce causality within the CFD solver. While the additive factorization is straightforward to solve numerically, the multiplicative factorization is more complicated. A numerical solution for the multiplicative factorization was provided in Martini et al. [2022]. The solution of the multiplicative factorization can be independently formed as

$$\hat{\mathbf{G}}(\omega) \hat{\mathbf{w}}_{i,+}(\omega) = \hat{\mathbf{w}}_{i,-}(\omega), \quad (\text{B.10})$$

where

$$\hat{\mathbf{G}}_{-}(\omega) = [\hat{w}_{1,-}(\omega), \hat{w}_{2,-}(\omega), \dots, \hat{w}_{n_{freq},-}(\omega)], \quad (\text{B.11a})$$

$$\hat{\mathbf{G}}_{+}(\omega) = [\hat{w}_{1,+}(\omega), \hat{w}_{2,+}(\omega), \dots, \hat{w}_{n_{freq},+}(\omega)]^{-1}, \quad (\text{B.11b})$$

where $\hat{\mathbf{G}} \in \mathbb{C}^{n_y \times n_y \times n_{freq}}$ or $\hat{\mathbf{G}} \in \mathbb{C}^{n_a \times n_a \times n_{freq}}$. To solve (B.10), a Fredholm integral equation of the second kind [Daniele and Lombardi, 2007] is derived as

$$\hat{\mathbf{x}}_i(\omega) + \frac{1}{2\pi i} \int_{-\infty}^{\infty} \frac{\hat{\mathbf{G}}^{-1}(\omega) \hat{\mathbf{G}}(u) - 1}{u - \omega} \hat{\mathbf{x}}_i(u) du = \hat{\mathbf{G}}^{-1}(\omega) \frac{\hat{\mathbf{w}}_{i,-}(\omega_0)}{\omega - \omega_0}. \quad (\text{B.12})$$

Due to the difficulty of the formation of the integration path, Martini et al. [2022] constructed a linear problem with the size $\mathbf{G} \in \mathbb{C}^{n_y \times n_y \times n_{freq}}$, given by

$$\hat{\mathbf{x}}_i(\omega) + \frac{1}{2i} \mathcal{H}(\hat{\mathbf{x}}_i)(\omega) - \frac{1}{2i} \hat{\mathbf{G}}^{-1}(\omega) \mathcal{H}(\hat{\mathbf{G}} \hat{\mathbf{x}}_i)(\omega) = \hat{\mathbf{G}}^{-1}(\omega) \frac{\hat{\mathbf{w}}_{i,-}(\omega_0)}{\omega - \omega_0}, \quad (\text{B.13})$$

where

$$\mathcal{H}(\hat{\mathbf{x}}) = P.V. \frac{1}{\pi} \int_{-\infty}^{\infty} \frac{1}{\omega - u} \hat{\mathbf{x}}(u) du, \quad (\text{B.14})$$

represents the Hilbert transform of $\hat{\mathbf{x}}(\omega)$. Equation (B.14) can be solved using the Generalized Minimal Residual (GMRES) iterative method [Saad and Schultz, 1986]. We solve (B.14) directly within the solver to minimize reliance on post-processing tools such as MATLAB and to enhance computational efficiency by enabling faster routines with reduced memory usage.

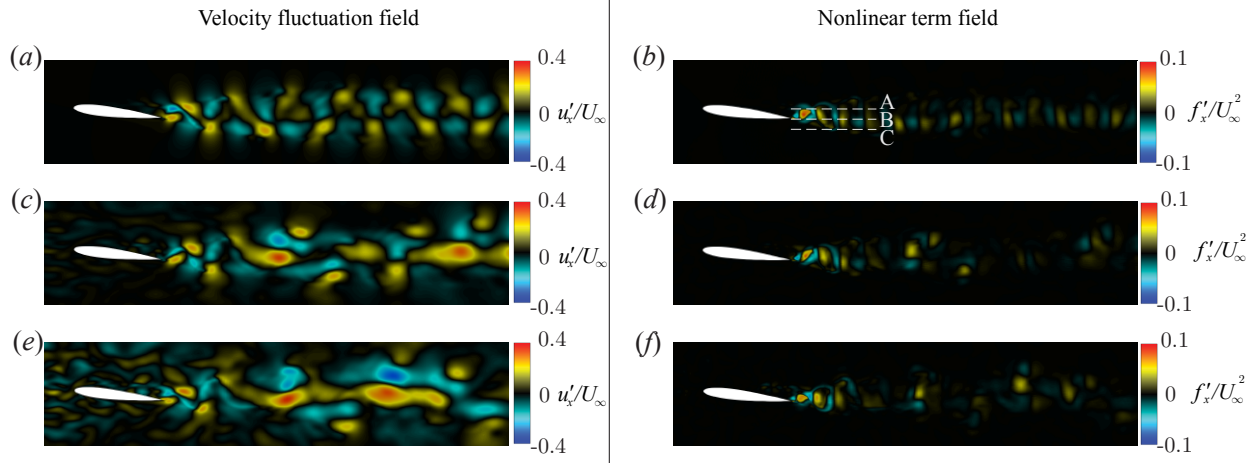


FIGURE 34: Instantaneous velocity fluctuation field u'_x ((a)(c)(e)) and the corresponding nonlinear terms f'_x ((b)(d)(f)) computed from 6.3. (a), (b): no forcing ($W = 0$); (c), (d): $W = 1$; and (e), (f): $W = 3$.

Appendix C Statistics of the nonlinear terms

We explore how much the nonlinearity interaction is developed from the external forcing \mathbf{F}_{ext} for the laminar airfoil flow with the intensity of the external disturbance. If the intensity of the external forcing is sufficiently small, (5.13) is approximately equivalent to (5.14). Figure 34 illustrates the instantaneous streamwise velocity fluctuations u'_x field with $W = [0, 1, 3]$ in (a), (c), and (e), and the corresponding the same time step's nonlinear terms in (b), (d), and (f). The nonlinear terms are extracted using our application §6.3. The clean system ($W = 0$) shown in figure 34(a) and (b) and the noisy systems ($W = [1, 3]$) depicted in figures 34(c) - (f) demonstrate that nonlinear terms predominantly exist in the wake near the trailing edge and in regions where the gradients of the velocity component are significant.

Figure 35 presents the PSDs and the CSDs at vortex shedding frequency ($St_\alpha = 0.17$) of the nonlinear terms along lines A ($y/L_c = 0.01$), B ($y/L_c = -0.11$), and C ($y/L_c = -0.21$) behind the airfoil, shown in figure 34(b). In figure 35(a)–(c), the nonlinear terms exhibit significant energy at the vortex-shedding frequencies. Strong energy is observed near the trailing edge ($x/L_c < 1.5$) along the top (A) and middle (B) lines, as shown in figures 35(a) and (b), while the bottom line (C) shows energetic regions further downstream, as seen in figure 35(c). This pattern arises because vortex shedding primarily originates from the separated flow on the suction surface, located slightly above the trailing edge. In figures 35(d)–(i), the nonlinear terms for both velocity components exhibit statistically significant strength in the region $1 < x/L_c < 1.2$ along line B, consistent with the observed deterioration in the estimation performance of the linear system. Examining the CSD tensors $\hat{\mathbf{F}}_{nl}$ is meaningful, as they are closely associated with coherent structures [Towne et al., 2018]. By constructing the forcing CSD matrix $\hat{\mathbf{F}}_{nl}$, we can account for the nonlinear effects of the flow in the estimation kernels, potentially improving estimation accuracy in turbulent flows.

Appendix D Sensor placement for estimation

Based on the single-sensor results reported in §7.2.3, we propose several candidates for the most effective sensor placement or multiple sensors, shown in table 3. The targets are averaged points of interest for both clean and noisy nonlinear systems. We verified that the estimator can improve accuracy when the sensor is at the trailing edge. However, this configuration is impractical for the control problem, which will be discussed

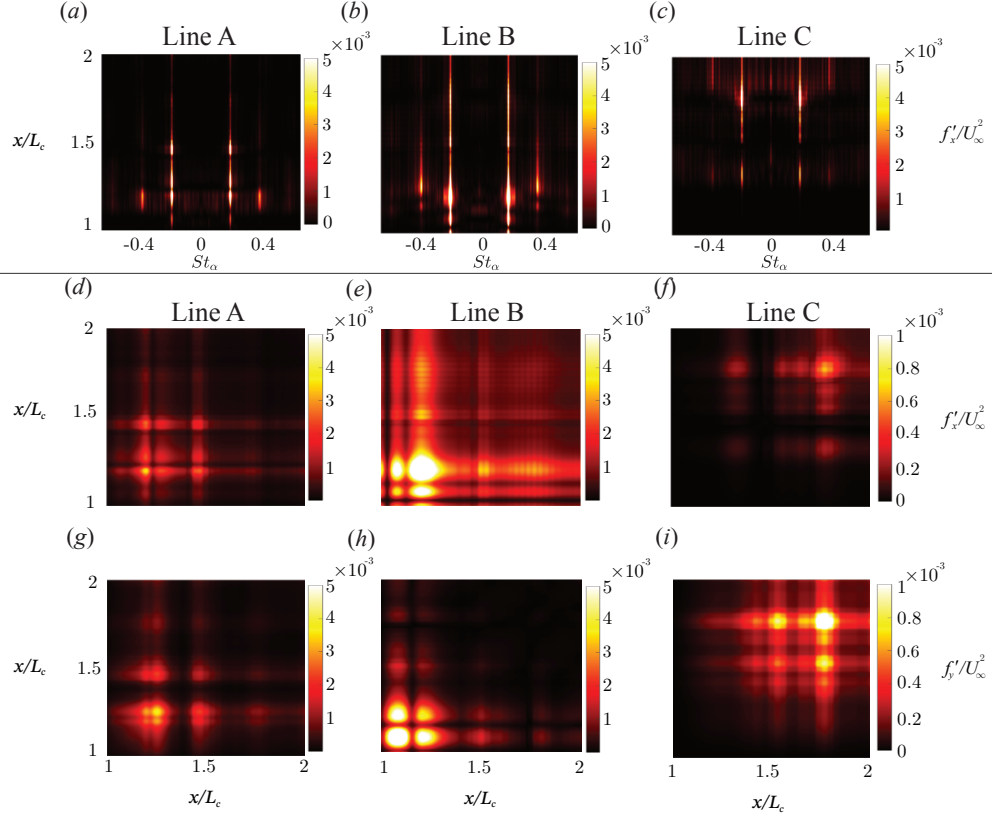


FIGURE 35: Power Spectral Densities (PSDs) and Cross-Spectral Densities (CSDs) of the nonlinear terms. The top three panels (a)–(c) display PSDs along Lines A, B, and C in figure 34(b). Panels (d)–(f) show the CSDs of f'_x , and panels (g)–(i) present the CSDs of f'_y for each corresponding line.


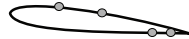

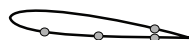


	Placement candidates	Errors	
		Clean system	Noisy system
1		0.04	0.54
2		0.03	0.40
3		0.02	0.36
4		0.01	0.35
5		0.001	0.33
6		0.001	0.33

TABLE 3: Sensor placement candidates for causal resolvent-based estimation.

in the upcoming section. Ultimately, We adopted candidate 6 in table 3, where sensors are located upstream of the separation bubble on the suction surface and near the trailing edge on both the suction and pressure

surfaces for estimation. The mathematical formulations for determining the optimal sensor placement are beyond the scope of this study and will be addressed in future research.

References

- B. R. Agrawal, A. Rosenberg, and A. Sharma. Towards identifying contribution of wake turbulence to inflow noise from wind turbines. *E3S Web Conf.*, 5:01002, 2015. ISSN 2267-1242. doi: 10.1051/e3sconf/20150501002.
- M. M. Alam, Y. Zhou, H. X. Yang, H. Guo, and J. Mi. The ultra-low reynolds number airfoil wake. *Exp. Fluids*, 48(1):81–103, January 2010. ISSN 0723-4864, 1432-1114. doi: 10.1007/s00348-009-0713-7.
- F. R. Amaral, A. V. G. Cavalieri, E. Martini, P. Jordan, and A. Towne. Resolvent-based estimation of turbulent channel flow using wall measurements. *J. Fluid Mech.*, 927:A17, November 2021. ISSN 0022-1120, 1469-7645. doi: 10.1017/jfm.2021.764.
- X. An, D. R. Williams, J. D. Eldredge, and T. Colonius. Lift coefficient estimation for a rapidly pitching airfoil. *Exp. Fluids*, January 2021.
- K. J. Asztalos, S. T. M. Dawson, and D. R. Williams. Modeling the flow state sensitivity of actuation response on a stalled airfoil. *AIAA J.*, pages 1–15, April 2021. ISSN 0001-1452, 1533-385X. doi: 10.2514/1.J060304.
- D. B. S. Audiffred, A. V. G. Cavalieri, P. P. C. Brito, and E. Martini. Experimental control of tollmien-schlichting waves using the wiener-hopf formalism. *Phys. Rev. Fluids*, 8(7):073902, July 2023. ISSN 2469-990X. doi: 10.1103/PhysRevFluids.8.073902.
- S. Bagheri, L. Brandt, and D. S. Henningson. Input–output analysis, model reduction and control of the flat-plate boundary layer. *J. Fluid Mech.*, 620:263–298, February 2009. ISSN 0022-1120, 1469-7645.
- S. Balay, S. Abhyankar, M. Adams, J. Brown, P. Brune, K. Buschelman, L. Dalcin, A. Dener, V. Eijkhout, W. Gropp, and Others. *Petsc users manual. Argonne Natl. Lab.*, 2019.
- R. Bhagwat. *Development of Stability Analysis Tools for High Speed Compressible Flows*. PhD thesis, North Carolina State University, 2020.
- R. Broglia, K.-S. Choi, P. Houston, L. Pasquale, and P. Zanchetta. Output feedback control of flow separation over an aerofoil using plasma actuators. *Int. J. Numer. Anal. Model.*, 15, 2018.
- S. L. Brunton and B. R. Noack. Closed-loop turbulence control: Progress and challenges. *Appl. Mech. Rev.*, 67(5), September 2015. ISSN 0003-6900, 2379-0407.
- G. A. Brès, F. E. Ham, J. W. Nichols, and S. K. Lele. Unstructured large-eddy simulations of supersonic jets. *AIAA J.*, 55:1164–1184, April 2017. ISSN 0001-1452, 1533-385X.
- J. Chang, Q. Zhang, L. He, and Y. Zhou. Shedding vortex characteristics analysis of naca 0012 airfoil at low reynolds numbers. *Energy Rep.*, 8:156–174, July 2022. ISSN 2352-4847. doi: 10.1016/j.egy.2022.01.149.
- Boa-Teh Chu. On the energy transfer to small disturbances in fluid flow (part i). *Acta Mechanica*, 1:215–234, September 1965. ISSN 0001-5970, 1619-6937.
- C. H. Colburn, J. B. Cessna, and T. R. Bewley. State estimation in wall-bounded flow systems. part 3. the ensemble kalman filter. *J. Fluid Mech.*, 682:289–303, September 2011. ISSN 0022-1120, 1469-7645.
- T. Colonius and D. R. Williams. Control of vortex shedding on two- and three-dimensional aerofoils. *Philos. Trans. R. Soc. A*, 369(1940):1525–1539, April 2011. ISSN 1364-503X, 1471-2962. doi: 10.1098/rsta.2010.0355.
- D. A. Cook, J. Thome, J. M. Brock, J. W. Nichols, and G. V. Candler. *Understanding Effects of Nose-Cone Bluntness on Hypersonic Boundary Layer Transition Using Input-Output Analysis*. 2018. doi: 10.2514/6.2018-0378.

- V. Daniele and G. Lombardi. Fredholm factorization of wiener-hopf scalar and matrix kernels. *Radio Sci.*, 42(6):2007RS003673, December 2007. ISSN 0048-6604, 1944-799X. doi: 10.1029/2007RS003673.
- T. Déda, W. Wolf, and S. Dawson. Neural networks in feedback for flow analysis, sensor placement and control, August 2023. arXiv:2308.13029 [physics].
- N. Fabbiane, O. Semeraro, S. Bagheri, and D. S. Henningson. Adaptive and model-based control theory applied to convectively unstable flows. *Appl. Mech. Rev.*, 66:060801, November 2014. ISSN 0003-6900, 2379-0407.
- N. Fabbiane, B. Simon, F. Fischer, S. Grundmann, S. Bagheri, and D. S. Henningson. On the role of adaptivity for robust laminar flow control. *J. Fluid Mech.*, 767:R1, March 2015. ISSN 0022-1120, 1469-7645.
- N. Fabbiane, S. Bagheri, and D. S. Henningson. Energy efficiency and performance limitations of linear adaptive control for transition delay. *J. Fluid Mech.*, 810:60–81, January 2017. ISSN 0022-1120, 1469-7645.
- A. Farghadan, E. Martini, and A. Towne. Scalable resolvent analysis for three-dimensional flows, September 2023. arXiv:2309.04617 [physics].
- A. Farghadan, J. Jung, R. Bhagwat, and A. Towne. Efficient harmonic resolvent analysis via time stepping. *Theor. Comput. Fluid Dyn.*, May 2024. ISSN 0935-4964, 1432-2250. doi: 10.1007/s00162-024-00694-1.
- J. E. Ffowcs Williams and B. C. Zhao. The active control of vortex shedding. *J. Fluids Struct.*, 3(2):115–122, March 1989. ISSN 0889-9746. doi: 10.1016/S0889-9746(89)90026-1.
- D. P. M. Fosas, D. Sipp, and P. J. Schmid. Efficient evaluation of the direct and adjoint linearized dynamics from compressible flow solvers. *J. Comput. Phys.*, 231(23):7739–7755, October 2012. ISSN 0021-9991. doi: 10.1016/j.jcp.2012.06.038.
- M. Frigo and S. G. Johnson. The design and implementation of fftw3. *Proc. IEEE*, 93(2):216–231, February 2005. ISSN 0018-9219. doi: 10.1109/JPROC.2004.840301.
- N. Fujisawa, Y. Kawaji, and K. Ikemoto. Feedback control of vortex shedding from a circular cylinder by rotational oscillations. *J. Fluids Struct.*, 15(1):23–37, Jan 2001. ISSN 0889-9746. doi: 10.1006/jfls.2000.0323.
- D. F. Gomez, F. Lagor, P. B. Kirk, A. Lind, A. R. Jones, and D. A. Paley. Unsteady dmd-based flow field estimation from embedded pressure sensors in an actuated airfoil. In *AIAA SCITECH Forum*, January 2019. ISBN 978-1-62410-578-4.
- S. Gottlieb and C. Shu. Total variation diminishing runge-kutta schemes. *Math. Comput.*, 67:73–85, 1998.
- A. Gross, C. Marks, and R. Sondergaard. Laminar separation control for eppler 387 airfoil based on resolvent analysis. *AIAA J.*, 62(4):1487–1502, April 2024. ISSN 0001-1452, 1533-385X. doi: 10.2514/1.J063492.
- P. Huerre and P. A. Monkewitz. Local and global instabilities in spatially developing flows. *Annu. Rev. Fluid Mech.*, 1990.
- J. Jeun, J. W. Nichols, and M. R. Jovanović. Input-output analysis of high-speed axisymmetric isothermal jet noise. *Phys. Fluids*, 28(4):047101, April 2016.
- B. Jin, S. J. Illingworth, and R. D. Sandberg. Feedback control of vortex shedding using a resolvent-based modelling approach. *J. Fluid Mech.*, 897:A26, August 2020. ISSN 0022-1120, 1469-7645. doi: 10.1017/jfm.2020.347.
- M. R. Jovanović and B. Bamieh. Componentwise energy amplification in channel flows. *J. Fluid Mech.*, 534:145–183, June 2005. ISSN 0022-1120, 1469-7645. doi: 10.1017/S0022112005004295.
- J. Jung. Resolvent-based estimation and control of aerodynamic flows. *PhD thesis*, 2024.
- R. E. Kalman. A new approach to linear filtering and prediction problems. *J. Basic Engng*, 82:35–45, 1960.
- Y. Kojima, C. Yeh, K. Taira, and M. Kameda. Resolvent analysis on the origin of two-dimensional transonic buffet. *J. Fluid Mech.*, 885:R1, February 2020. ISSN 0022-1120, 1469-7645.

- C. Leclercq, F. Demourant, C. Poussot-Vassal, and D. Sipp. Linear iterative method for closed-loop control of quasiperiodic flows. *J. Fluid Mech.*, 868:26–65, June 2019. ISSN 0022-1120, 1469-7645. doi: 10.1017/jfm.2019.112.
- C. Lin and H. Tsai. Feedback flow control on a plunging circular cylinder. *Phys. Fluids*, 36(4):047126, April 2024. ISSN 1070-6631, 1089-7666. doi: 10.1063/5.0203558.
- O. Marquet, J.S. Leontini, J. Zhao, and M.C. Thompson. Hysteresis of two-dimensional flows around a NACA0012 airfoil at $Re = 5000$ and linear analyses of their mean flow. *Intl. J. Heat and Fluid Flow*, 94: 108920, April 2022. ISSN 0142727X.
- F. Martinelli. Feedback control of turbulent wall flows. *PhD thesis*, 2009.
- E. Martini, A. V. G. Cavalieri, P. Jordan, A. Towne, and L. Lesshafft. Resolvent-based optimal estimation of transitional and turbulent flows. *J. Fluid Mech.*, 900:A2, October 2020. ISSN 0022-1120, 1469-7645.
- E. Martini, J. Jung, A. Cavalieri, P. Jordan, and A. Towne. Resolvent-based tools for optimal estimation and control via the wiener–hopf formalism. *J. Fluid Mech.*, 937:A19, April 2022.
- B. J. McKeon and A. S. Sharma. A critical-layer framework for turbulent pipe flow. *J. Fluid Mech.*, 658: 336–382, September 2010.
- C. Min and H. Choi. Suboptimal feedback control of vortex shedding at low reynolds numbers. *J. Fluid Mech.*, 401:123–156, December 1999. ISSN 0022-1120, 1469-7645. doi: 10.1017/S002211209900659X.
- P. Morra, K. Sasaki, A. Hanifi, A. V. G. Cavalieri, and D. S. Henningson. A realizable data-driven approach to delay bypass transition with control theory. *J. Fluid Mech.*, 883:A33, January 2020. ISSN 0022-1120, 1469-7645. doi: 10.1017/jfm.2019.793.
- Pierluigi Morra, Petrônio A. S. Nogueira, André V. G. Cavalieri, and Dan S. Henningson. The colour of forcing statistics in resolvent analyses of turbulent channel flows. *J. Fluid Mech.*, 907:A24, 2021. doi: 10.1017/jfm.2020.802.
- E. J. Nielsen and W. L. Kleb. Efficient construction of discrete adjoint operators on unstructured grids using complex variables. *AIAA J.*, 44(4):827–836, 2006. doi: 10.2514/1.15830.
- Bernd R. Noack, Konstantin Afanasiew, Marek Morzynski, Gilead Tadmor, and Frank Thiele. A hierarchy of low-dimensional models for the transient and post-transient cylinder wake. *J. Fluid Mech.*, 497:335–363, 2003. doi: 10.1017/S0022112003006694.
- B. Noble. *Methods Based on the Wiener-Hopf Technique for the Solution of Partial Differential Equations*, volume 7 of *Int. Ser. Monogr. Pure Appl. Math.* Pergamon Press, New York, 1958.
- L. Pasquale, R. Broglia, K.-S. Choi, D. Durante, and P. Zanchetta. Robust control of flow separation over a pitching aerofoil using plasma actuators. *IFAC-PapersOnLine*, 50(1):11120–11125, July 2017. ISSN 2405-8963.
- M. Rafiee, Q. Wu, and A. M. Bayen. Kalman filter based estimation of flow states in open channels using lagrangian sensing. In *Proceedings of the 48th IEEE Conference on Decision and Control (CDC)*, pages 8266–8271. IEEE, December 2009. ISBN 978-1-4244-3871-6.
- J. H. M. Ribeiro, C. Yeh, and K. Taira. Randomized resolvent analysis. *Phys. Rev. Fluids*, 5(3):033902, March 2020. ISSN 2469-990X. doi: 10.1103/PhysRevFluids.5.033902.
- K. Roussopoulos and P. A. Monkewitz. Nonlinear modelling of vortex shedding control in cylinder wakes. *Phys. D Nonlinear Phenom.*, 97(1-3):264–273, October 1996. ISSN 0167-2789. doi: 10.1016/0167-2789(96)00151-0.
- Y. Saad and M. H. Schultz. GMRES: A generalized minimal residual algorithm for solving nonsymmetric linear systems. *SIAM J. Sci. Stat. Comput.*, 7(3):856–869, July 1986. ISSN 0196-5204, 2168-3417. doi: 10.1137/0907058.

- K. Sasaki, P. Morra, N. Fabbiane, A. V. G. Cavalieri, A. Hanifi, and D. S. Henningson. On the wave-cancelling nature of boundary layer flow control. *Theor. Comput. Fluid Dyn.*, 32:593–616, October 2018a. ISSN 0935-4964, 1432-2250.
- K. Sasaki, G. Tissot, A. V. G. Cavalieri, F. J. Silvestre, P. Jordan, and D. Biau. Closed-loop control of a free shear flow: A framework using the parabolized stability equations. *Theor. Comput. Fluid Dyn.*, 32(6): 765–788, December 2018b. ISSN 0935-4964, 1432-2250. doi: 10.1007/s00162-018-0477-x.
- P. J. Schmid and D. Sipp. Linear control of oscillator and amplifier flows. *Phys. Fluids*, 1:040501, August 2016. ISSN 2469-990X.
- O. T. Schmidt and A. Towne. An efficient streaming algorithm for spectral proper orthogonal decomposition. *Comput. Phys. Commun.*, 237:98–109, April 2019. ISSN 0010-4655. doi: 10.1016/j.cpc.2018.11.009.
- O. T. Schmidt, A. Towne, G. Rigas, T. Colonius, and G. A. Brès. Spectral analysis of jet turbulence. *J. Fluid Mech.*, 855:953–982, November 2018. ISSN 0022-1120, 1469-7645.
- A. Sharma, D. Limebeer, B. McKeon, and J. Morrison. Stabilising control laws for the incompressible navier-stokes equations using sector stability theory. In *3rd AIAA Flow Control Conf.*, San Francisco, California, June 2006. AIAA. ISBN 978-1-62410-036-9. doi: 10.2514/6.2006-3695.
- D. Sipp, O. Marquet, P. Meliga, and A. Barbagallo. Dynamics and control of global instabilities in open-flows: A linearized approach. *Appl. Mech. Rev.*, 63(3):030801, May 2010. ISSN 0003-6900, 2379-0407. doi: 10.1115/1.4001478.
- Robert F. Stengel. *Optimal Control and Estimation*. Dover Publ., 1994.
- P. J. Strykowski and K. R. Sreenivasan. On the formation and suppression of vortex ‘shedding’ at low reynolds numbers. *J. Fluid Mech.*, 218:71, September 1990. ISSN 0022-1120, 1469-7645. doi: 10.1017/S0022112090000933.
- S. Symon, D. Sipp, and B. J. McKeon. A tale of two airfoils: resolvent-based modelling of an oscillator versus an amplifier from an experimental mean. *J. Fluid Mech.*, 881:51–83, December 2019. ISSN 0022-1120, 1469-7645. doi: 10.1017/jfm.2019.747.
- J. S. Tao, X. Y. Huang, and W. K. Chan. A flow visualization study on feedback control of vortex shedding from a circular cylinder. *J. Fluids Struct.*, 10(8):965–970, November 1996. ISSN 0889-9746. doi: 10.1006/jfls.1996.0061.
- N. Thomareis and G. Papadakis. Resolvent analysis of separated and attached flows around an airfoil at transitional reynolds number. *Phys. Rev. Fluids*, 3:073901, July 2018. ISSN 2469-990X.
- A. Towne, G. A. Brès, and S. K. Lele. A statistical jet-noise model based on the resolvent framework. *AIAA Paper #2017-3406*, 2017.
- A. Towne, O. T. Schmidt, and T. Colonius. Spectral proper orthogonal decomposition and its relationship to dynamic mode decomposition and resolvent analysis. *J. Fluid Mech.*, 847:821–867, July 2018.
- A. Towne, A. Lozano-Durán, and X. Yang. Resolvent-based estimation of space–time flow statistics. *J. Fluid Mech.*, 883:A17, January 2020. ISSN 0022-1120, 1469-7645.
- S. Wagner, R. Bareiß, and G. Guidati. *Wind Turbine Noise*. Springer-Verlag, 1996.
- P. Welch. The use of fast fourier transform for the estimation of power spectra: A method based on time averaging over short, modified periodograms. *IEEE Trans. Audio Electroacoust.*, 15(2):70–73, June 1967. ISSN 0018-9278.
- C. Yeh and K. Taira. Resolvent-analysis-based design of airfoil separation control. *J. Fluid Mech.*, 867: 572–610, May 2019. ISSN 0022-1120, 1469-7645.
- A. Zare, M. R. Jovanović, and T. T. Georgiou. Colour of turbulence. *J. Fluid Mech.*, 812:636–680, February 2017. ISSN 0022-1120, 1469-7645. doi: 10.1017/jfm.2016.682.